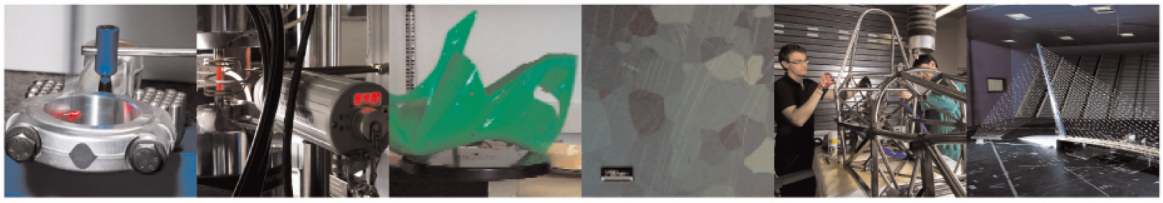

Hybrid thermal, mechanical and chemical surface post-treatments for improved fatigue behavior of laser powder bed fusion AlSi10Mg notched samples

Maleki E.;Bagherifard S.;Sabouri F.;Bandini M.;Guagliano M.

This is a post-peer-review, pre-copyedit version of an article published in Surface and Coatings Technology. The final authenticated version is available online at:
https://doi.org/10.1016/j.surfcoat.2021.127962

DIPARTIMENTO DI MECCANICA ■ POLITECNICO DI MILANO
via G. La Masa, 1 ■ 20156 Milano ■ EMAIL (PEC): pecmecc@cert.polimi.it
http://www.mecc.polimi.it
Rev. 0

Hybrid thermal, mechanical and chemical surface post-treatments for improved fatigue behavior of laser powder bed fusion AlSi10Mg samples with notched geometry

Erfan Maleki[a], Sara Bagherifard[a*], Farshad Sabouri[a], Michele Bandini[b], Mario Guagliano[a]
[a] Department of Mechanical Engineering, Politecnico di Milano, Milano, Italy
[b] Peen Service srl, Bologna, Italy

*Corresponding author, Email: sara.bagherifard@polimi.it

Abstract
Complex geometries can be produced by laser powder bed fusion (LPBF) techniques in a layer-by-layer manner. These parts exhibit inhomogeneous microstructure and poor surface quality in their as-built state. Performing post-treatments to modify these imperfections can play a substantial role in enhancing the performance of LPBF parts. However, the effects of post treatments on local geometrical irregularities are not still well documented. In this study, four different post-treatments including heat treatment, mechanical and chemical surface treatments as well as their combination were considered. Their effect was studied on microstructure, surface, and mechanical properties of LPBF V-notched AlSi10Mg samples. The as-built samples were subjected to two different shot peening processes (using different Almen intensity, shot diameter, and shot hardness), chemical polishing and electro-chemical polishing, in individual and combined configurations. Comprehensive microstructural characterization was carried out and the surface state of the samples was studied in detail in terms of surface morphology and roughness. In addition, mechanical properties including microhardness and residual stresses were measured and finally fatigue behaviors of the samples were determined and compared at a constant stress level. All post treatmemnts led to improved fatigue life. The combination of the aforementioned post-treatments led to a remarkable fatigue life improvement up to 414 times compared to the as-built state.
Keywords: laser powder bed fusion (LPBF), shot peening, heat treatment, chemical polishing, fatigue, notch, AlSi10Mg

1. Introduction
Laser powder bed fusion (LPBF) is one of the most widely used additive manufacturing (AM) technologies, used to fabricate mechanical components with intricate geometries. LPBF metallic materials, due to the complex physical phenomena of melting, solidification and rapid cooling occurring during the fabrication process are characterized with different types of surface and bulk defects [1]. These materials exhibit highly inhomogeneous and anisotropic microstructures [2], internal and sub-surface porosities [3], high tensile residual stresses [4,5], and quite poor surface quality [6], in their as-built state. Internal defects and pores form by the entrapment of inert gas in the melt pool during the melting of powder [7,8], or due to the lack of fusion caused by insufficient choosing of the LPBF process parameters such as high laser power and scanning speed [9]. Surface related imperfections characterized by irregular and randomly positioned surface features, are mainly caused by the presence of partially melted or unmelted feed-stock, spatters, balling effects, melt-pool instability, stair-case effects, and support removal [6,8,10,11]. In addition, geometrical features and orientation of specific surfaces with respect to the build direction have defining roles on the surface quality of LPBF parts in terms of roughness and irregularities.
Each AM technology can be controlled by a set of specific parameters known as process parameters the alteration of which directly affects the properties of the fabricated material in terms of internal and surface quality [12]. Considerable effort has been recently put into the investigation of the role of process parameters in LPBF technology to obtain their optimal range for fabrication of Al alloys [13–16]. The process parameter optimization has been mostly performed with the aim to modulate a specific physical or

mechanical property such as porosity, yield and ultimate tensile strength, hardness and surface roughness. However, once the fabrication process is optimized to minimize the remaining surface and bulk defects that could not be addressed due to the technological limits, post-treatments can come into play to address the shortcomings related to the surface state of the samples.

The defects of as-built AM material and in particular the presence of irregular and inhomogeneous surface features act as stress concentration sites causing early crack initiation [17–19], which directly affect the load bearing properties of the AM materials especially under cyclic loading [20,21]. Therefore, application of post-treatments on AM parts can play a crucial role in modifying their mechanical performance. Dealing with internal defects, heat treatment (HT) can be employed for relaxation of the tensile residual stresses and homogenizing the microstructure; hot isostatic pressing (HIP) has been also used for reducing the internal porosities [22,23]. Regarding surface characteristics that have a defining role in mechanical performance of LPBF parts, as most of mechanical failures such as fatigue are remarkably sensitive to the surface properties, a wide range of post-treatments have been suggested [2,24–28]. Surface post-treatments for AM have been categorized into four major groups including treatments that are based on material removal, no material removal and coatings as well as hybrid treatments [29]. In the treatments based on material removal such as chemical treatments, desirable surface morphology can be obtained by removing a thin surface layer of material, without interfering with the other physical/microstructural properties of the AM material. Chemical post-treatments offer the possibility to reduce the surface roughness of an AM part especially those with complex geometries such as lattice and cellular structures as well as notched geometries. In this regard, different chemical treatments have been suggested including chemical etching [30–32], chemical machining [33], chemical brightening [33], chemical polishing (CP) [34,35] and electrochemical polishing (ECP) [36]. These chemical treatments are mostly similar and are all based on dipping the AM part in baths of chemical solutions. The differences are related to the process duration, temperature or voltage of the solution, which affect the extent of the material removal. For instance, Jung *et al.* [37] investigated the influence of ECP considering different times and voltages on surface properties of PBF pure Ti samples. The results indicated that ECP with 600 s and 30 V had the best performance for roughness reduction.

On the other hand, surface post-treatments based on no material removal such as shot peening (SP), induce homogeneous and regular surface morphological features besides other beneficial effects such as surface layer hardening and inducing compressive residual stresses [38], which can have remarkable effects on the improvement of mechanical properties and fatigue behaviour of the AM materials [17,39–46]. SP is a cold working process based on surface plastic deformation in which the target surface is impacted with a flow of small shots under controlled conditions [47–50]. It can considerably improve the surface and sub-surface properties in AM materials; however, the issues associate with bulk material cannot be tackled by SP. Thus, due to the requirements of the final applications, different post-treatments can be combined as hybrid treatments to obtain the desirable surface or bulk properties for AM metallic materials. Synergetic influences of SP combined with HT were studied on LPBF AlSi10Mg smooth fatigue samples, which revealed surface morphology modification and fatigue properties improvement [51]. Different combinations of post-treatments including HT, sand blasting (SB) and chemical etching were also performed on LPBF Ti-6Al-4V lattice parts which led to notable surface roughness reduction after applying hybrid treatment compared to as-built state [52].

Most studies till now have been dealing with smooth surfaces and standard geometries for AM fabricated samples. However, more intricate geometries, that are indeed the point of strength of AM, should be treated differently as they can respond to the post-treatments in a distinct way different from the smooth surfaces. Notched AM parts are known to represent a more inhomogeneous surface roughness depending on the orientation of the surfaces with respect to the build direction. Past studies have shown that the notch area especially on its downward face contains higher extent of surface imperfections that can have adverse effects on the part's fatigue behaviour [53–55]. Machining is a commonly used process for removing the surface irregularities of as-built blunt notched AM parts [56,57]. However, machining of sharp notches with small notch root radius is quite challenging if not impossible. Consequently, using other alternative surface post-treatments on the notched AM parts can represent a key to address the surface imperfection issues.

Following our previous study, which surveyed the effects of different post-treatments of HT, SP and their combination on fatigue strength of notched LPBF samples [58], in this study we investigated the effects of CP and ECP post-treatments applied on as-built and HT series, and compared the results also with those obtained after SP treatment, both separately and combined together, on microstructure, mechanical properties and fatigue behavior of LPBF V-notched AlSi10Mg samples. We studied the considered treatments on V-notched samples with the peculiarities that are associated with the upskin and downskin zones. Furthermore, the combination of different mechanical and chemical surface-post treatments together also provides additional insight on the efficiency of such treatments on inclined surfaces. For each of the individual post-treatments, two different set of parameters were considered. Two SP treatments performed by steel and ceramic shots with different Almen intensities; and two processes of chemical polishing (CP) and electro-chemical polishing (ECP) were applied. Comprehensive experimental tests including microstructural characterization, porosity and surface morphology analysis as well as mechanical characterization including rotating bending fatigue tests were performed on as-built and heat treated samples before and after applying SP, CP and ECP treatments.

2. Experimental procedure

2.1. Sample preparation

Gas atomized spherical powder of AlSi10Mg (SLM solutions Group AG, DE) with particle size of 20-63 µm and mean diameter of 46.65 µm was used for LPBF samples manufacturing. Table 1 shows the nominal chemical composition of the feedstock material. The samples were fabricated via SLM 500 HL systems (SLM Solution Group AG, DE) with Yttrium fiber lasers. LPBF process parameters included spot diameter of 78 µm, laser power of 350 W, and scan speed of 1150 mm /s, layer thickness of 50 µm and hatch distance of 170 µm. In this study, the LPBF process parameters are referenced to a previous work of the authors [51]. The parameters were optimized for the powder type and the SLM system used for the fabrication of the samples. Vertical direction considering a scanning strategy of 67° rotation between the layers and contour remelting were implemented. The relevant scanning strategy is depicted in Fig. 1a. The baseplate was pre-heated to 150 °C and the chamber was flooded with argon gas, keeping the oxygen content below 0.2% during the fabrication process. These parameters were optimized in a previous study performed by some of the authors [51]. Wire electrical discharge machining was used to detach the fabricated samples from the build plate. Cylindrical samples with V-shaped notches (elastic stress concentration factor (K_t) of 2.43) were produced. Fig. 1b illustrates the shape and size of the notched fatigue samples.

Table 1. Nominal chemical composition of AlSi10Mg powder

Element	Al	Si	Fe	Cu	Mn	Mg	Zn	Ti	Ni	Pb	Sn
Actual (wt%)	Balance	9.87±1	0.07	<0.01	0.002	0.35±0.15	<0.01	<0.01	<0.01	<0.01	<0.01

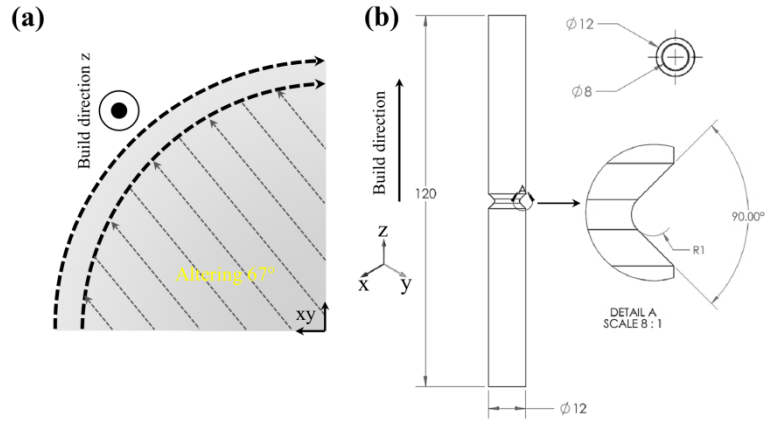

Fig.1. (a) Schematic illustration of scanning strategy used in this study. (b) Shape and size of the cylindrical V-notched fatigue sample with R1 notch root radius (all dimensions are presented in mm).

2.2. Post-treatments

Three different post-treatments were performed on the samples. The first one, HT, was aimed at modifying the microstructural and residual stresses, whereas the other two were surface treatments mainly dealing with surface imperfections.

T6 thermal treatment as a common treatment for Al alloys was performed on half of the samples according to the time and temperature intervals recommended by Aboulkhair *et al.* [59]. The final quenching step in water was considered according to the study carried out by Gharavi *et al.* [60] which followed the ASM standard [61]. The samples were heated up to 560 °C, solution heat treated for 1 h, quenched in water with a storage time of 1 h, followed by heating up to 160 °C and ageing for 6 h at 160 °C with final quenching in water [51].

Two different SP treatments were performed using different types of impacting media and also different Almen intensities. Table 2 represents the details of considered SP processes with steel and ceramic shots applied on both as-built and heat treated samples. Almen intensities were determined according to the SAE J443 standard [62]. The two SP treatments (SP1 and SP2) were performed on both as-built (AB) and heat treated (HT) samples. Hence six different sets of samples were considered to study the sole influence of each post-treatment as well as their hybrid conditions, i.e., AB, AB+HT, AB+SP1, AB+SP2, AB+HT+SP1and AB+HT+SP2.

Table 2. Details of the applied SP treatments on LPBF AlSi10Mg samples

SP treatment	Shot material	Shot hardness (HRC)	Shot standard category	Shot diameter (mm)	Almen intensity (A 0.001 inch)	Surface coverage (%)
SP1	Steel	48-50	S 170	0.43	10	100
SP2	Ceramic	60-62	Z 100	0.1-0.15	5	100

In addition, two different chemical treatments including CP and ECP were carried out on both as-built and heat treated series. As there is no available data in the literature about the optimized conditions of CP and ECP processes on LPBF AlSi10Mg, different process parameters were considered for both chemical treatments. 12 different conditions were designed for each CP and ECP on as-built state and then the optimized parameters were selected for both treatments in terms of highest roughness reduction.

In CP process, two parameters of temperature and time were considered to control the process. The CP experiments were performed using bath of solution of 900 mL H_2O + 200 g Nitrate (NO-3)+ 375 g NaOH in three different temperatures of 25°C (room temperature), 50°C and 75 °C and 4 different polishing times of 60 s, 120 s, 180 s and 240 s. In ECP treatments, two parameters of voltage and exposure time were

considered for controlling the process. ECPs were carried out using bath of 400 mL solution with 94% Acetic acid (CH_3COOH)+6% Perchloric ($HClO_4$) acid at three different voltages of 5 V, 10 V and 15 V and 4 different times of 60 s, 120 s, 180 s and 240 s. After the chemical treatments, the samples were immediately washed with water and then ultrasonically cleaned in a solution of 50% acetone and 50% desalinated water. Selected CP and ECP parameters were applied to as-built sample leading to two series of AB+CP and AB+ECP. Then, between the CP and ECP, the treatment that had the highest effect on fatigue behavior improvement of as-built state was chosen to apply on the other sets of heat treated and shot peened samples (mentioned above). Fig. 2 reveals the schematic illustration of the applied surface post-treatments in this study including SP, CP and ECP considering details of each process.

2.3. Tensile strength test

Monotonic tensile tests were carried out on dog-bone as-built and heat treated sets using three samples per each. The samples were tested following ISO 6892-1 on an MTS Alliance RT/100 machine at a strain rate of 0.7 mm/min up to 2% strain with constant rate of 2 mm/min. To measure the material elongation during the experiment, an extensometer was attached to the samples.

2.4. Microstructural characterization

Firstly, samples were cut in longitudinal and transversal sections with respect to the build direction and then were impregnated in hot mounting resin. The polishing steps were carried out with final step of polishing using silica suspensions. The polished cross-sections were chemically etched for 20 s in Keller's reagent (95% pure H_2O, 1% HF, 1.5% HCl, 2.5% HNO_3). The microstructural characterization was carried out using a Nikon Eclipse LV150NL optical microscope (OM, Nikon Corporation, Japan) and a high resolution Zeiss Sigma 500 VP field-emission scanning electron microscope (FE-SEM, Carl Zeiss Microscopy GmbH, Germany) equipped with energy dispersive spectrometry (EDS) and electron backscattered diffraction (EBSD). AZtecHKL software was used to process the EDS and EBSD data.

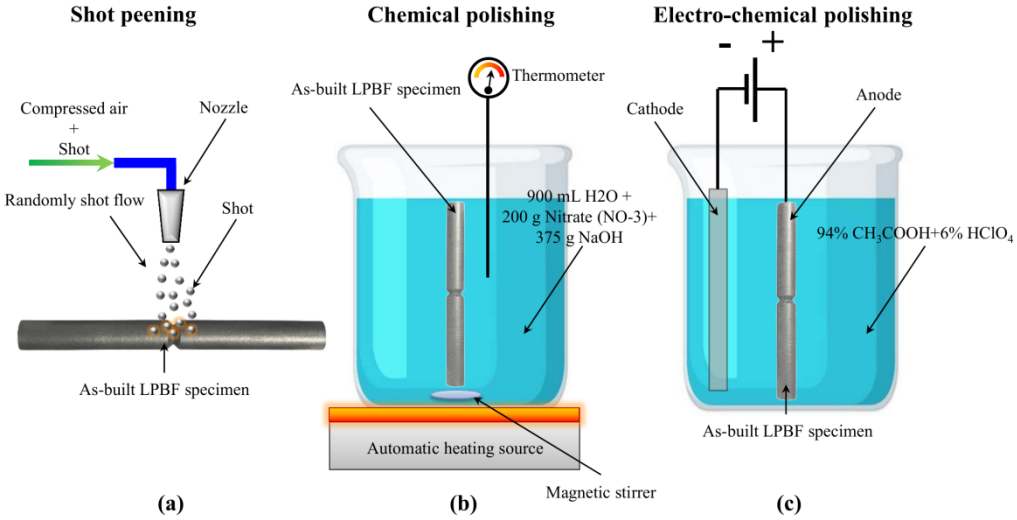

Fig. 2. Schematic illustration of the applied surface post-treatments in this study including (a) SP, (b) CP and (c) ECP.

2.5. Porosity measurement

Image based analyses were employed for porosity measurements on the notch area of the samples. Three different surfaces including top (*xy*-plane), middle (*yz*-plane) and bottom (*xy*-plane) surfaces of notch area were considered for SEM observations. Three back scattered electron SEM (BSE-SEM) images were taken from random areas of each polished surfaces. Three additional OM images were used for sub-surface porosity analysis of all sets of samples. ImageJ software [63] was employed for analyzing the BSE-SEM

micrographs. Also, the t-student test was utilized to obtain statistical significance between different sets of samples.

2.6. Surface roughness measurement and morphology observation

Surface roughness measurements were performed via Mahr Perthometer (PCMESS 7024357) equipped with MFW 250 probe with a tip diameter of 5 μm. EN ISO 4287 standard [64] was followed for sampling and cut-off wavelengths and the filtering parameters. Three samples were considered for each series and three measurements were applied on random surface areas of each. Average values of profile roughness parameters including arithmetic mean (R_a), root mean square (R_q), maximum height of the profile (R_t) and the mean maximum height (R_z) were obtained for each set. Surface morphological analysis were performed using a Zeiss EVO50 SEM on both the notch area and the smooth cylindrical area 1 cm above the notch. Before both surface roughness measurements and surface morphology observations, the samples were ultrasonically cleaned in a solution of 50% acetone and 50% desalinated water for 10 min.

2.7. Microhardness measurement

Microhardness tests were performed on finely polished cross-sections of samples using a Leica WMHT30A micro Vickers hardness tester. Loads of 25 gf and dwell time of 15 s were used for each indentation. Measurements were performed on transversal section (*xy*-plane) and 5 different paths were considered for each sample starting at a depth of 40 μm from the sub-surface towards the core material up to a depth of 740 μm with an interval distance of 50 μm.

2.8. Residual stress measurement

X-ray diffraction (XRD) was employed to obtain the distributions of residual stresses along a perpendicular path with respect to the build direction starting from top surface. AST X-Stress 3000 portable X-ray diffractometer with CrKα radiation, λK alpha 1 = 2.2898 Å, irradiated area of 4 mm diameter, and $\sin^2(\psi)$ method, was used. Diffraction angle (2θ) of 139° corresponding to {311}-reflex was scanned with a total of 7 Chi tilts between 45° and −45° along three rotations of 0°, 45°and 90° with a constant step size of 0.028°. Measurements were applied gradually by removing a very thin layer of material about 20 μm up to the depth of 200 μm; the step size was increased to 40 μm for depths> 200 μm; material removal was performed through electro-chemical polishing with a solution of acetic acid (94%) and perchloric acid (6%) at a voltage of 40 V for 45 s. Precision Mitutoyo micrometer (IDCH0530/05060) was used to determine the depth of material removal in each removing step. XRD is the most widely used method for residual stress measurements and also electro-polishing is mostly used for in-depth material removal as this method does not have any considerable effects on inducing other residual stresses if the process parameters are selected correctly [65,66].

2.9. Fatigue tests and fractography analysis

Fatigue behavior of LPBF V-notched AlSi10Mg were analyzed via rotating bending fatigue tests at a stress ratio of R=−1 at room temperature and air relative humidity of about 50%. Italsigma (IT) equipment with rotational speed around 2500 rpm was used. In order to compare the influence of the applied post-treatments on fatigue life of the notched samples, fatigue tests were performed at fixed amplitude stress of 110 MPa with a run-out limit set to 6×10^6 cycles for all sets. Three samples were tested at mentioned stress level and the average of obtained fatigue lives of each set is reported. In addition, fractography analysis was carried out on the failed samples STEREO discovery V12 Zeiss.

3. Results and discussions

3.1. Tensile test

Quasi-static mechanical properties of the AB and AB+HT samples were obtained using tensile test on three samples [51]. For AB series, the values of 72±1.5 GPa, 273±3 MPa, 393±20 MPa and 2.5±0.4 % were obtained for Young modulus, yield stress, ultimate stress and elongation, respectively. The AB+HT samples, on the other hand, exhibited tensile properties of 73±1 GPa, 201±6 MPa, 265±9 MPa and 13±1 %

for the aforementioned parameters, respectively. The results reveal the remarkable influence of the applied heat treatment, i.e., 5-fold higher elongation of the material and therefore high ductility improvement, even though the yield and ultimate strength were reduced. Grain growth occurred after heat treatment can be the major reason for the observed trend, which can be justified by Hall-Petch relation [67]. The elastic modulus in both AB and AB+HT samples were similar to the cast material reported in EN1706 [68]. The elongation of the AB series is also analogous to the cast material. The high yield and ultimate tensile strength of AB sample is related to the fine grain size caused by high cooling rate of about 10^6 K/s of melt pool occurring during the LPBF process [69,70].

3.2. Microstructural analysis

Different analyses using OM, FESEM, EBSD and XRD were performed for microstructural characterization of the LPBF AlSi10Mg. Firstly, the AB and AB+HT samples were investigated in detail and then the plastically deformed surface layers of the shot peened samples were analyzed. Fig. 3 presents the microstructural observations for AB and AB+HT samples. Fig. 3a, reveals the comparison of the general microstructure of the AB and AB+HT samples in transversal (*xy*-plane) and longitudinal (*yz*-plane) cross sections obtained by OM. In longitudinal section of AB, the melt pool morphologies and hatching lines are clear and grains elongated along the build direction can be observed. Whereas micrographs from the transversal section of AB, exhibit the melt pool tracks and the inhomogeneous microstructure orientated following the 67° rotation strategy implemented between the subsequent layers. On the AB+HT sample, on the other hand, melt pool morphologies and hatching traces are mostly faded leading to a notable homogeneity in both cross-sections. Also, spherical and irregular pores can be seen in both AB and AB+HT samples.

Fig.3b illustrates the FESEM observations of AB and AB+HT samples on their longitudinal cross-sections (*yz*-plane). In AB sample, fibrous Si networks surrounded by α-Al matrix can be observed; while in the AB+HT sample, remarkable homogeneity was obtained by transformation of the Si networks to Si spherical particles that were homogeneously dispersed in the Al matrix, as also previously reported by Wei *et al.* [71]. Also, needle-like Mg_2Si precipitates formed after T6 heat treatment [72,73], are present in the Al matrix. In addition, EDS elements maps corresponding to the FESEM scanned area for both AB and AB+HT samples are shown in Fig. 3b; these maps clearly indicate the segregation of Si particles spread in boundaries of α-Al matrix in AB+HT sample.

Fig. 3c represntes the output of EBSD analyses in transversal cross-sections (*xy*-plane) of AB and AB+HT samples. The band contrast images hughlight a remarkable inhomogenity in grains morphology for the AB sample in comparison with the AB+HT one. As the solidification of grains in LPBF AlSi10Mg is facilitated along the build direction (*z*-dirction) due to epitaxial growth [74,75], the *z*-direction was considered for EBSD inverse pole figures (IPF-*Z*) maps based on crystallographic parameters of the Al phase. Epitaxial growth of grain is occured within solidification as a consequence of directional heat transfer in LPBF fabricated materials [76]. Si phase was not considered for diffraction to avoid interference with Al and also to get highest resolution. In the IPF-Z maps randomly orientation of the grains are can be seen, but grains oriented along (001) (parallel to the build) direction are dominating in both AB and AB+HT samples. In the AB sample relatively small equiaxed grains were formed mostly along the melt pool boundary, which is a common phenomenon in LPBF AlSi10Mg [77]. This is mainly due to variation of cooling rate at the centre and boundaries of melt pool. The applied heat treatment is noted to cause grain growth in the samples.

Fig. 4a depicts the XRD patterns of all sets of samples and Fig. 4b illustrates the primary and secondary peaks of the XRD patterns. Compared to the as-built and heat treated states, the intensities of the primary and secondary peaks are enhanced in the shot peened samples and the peaks are shifted towards different diffraction angles. The presence of Mg_2Si peak confirms the FESEM observations. Mg_2Si peak intensities are not so high due to the low content of Mg (0.35 wt%) in the feedstock alloy. In addition texture coefficient analysis was carried out using Harris' equation, which calculates the degree of preferred orientation through ratios between the measured peak intensities and database intensities for the same material [78], as shown in Fig. 4c. Texture coefficient of 1 is related to material's database and the texture coefficient of 3.5 is

corresponding to the complete preferred orientation in the plane. Peaks of Al (111), Al (200), Si (111), Si (311) and Mg_2Si (220) were considered. AB+HT+SP2 sample exhibited the highest texture coefficient with 3.24 in Al (200) followed by AB+HT+SP1, AB+SP2, AB, AB+SP1 and AB+HT samples with 2.53, 1.85, 1.42, 1.1 and 0.64, respectively; this observation indicates considerable shifts from the preferred orientation in the columnar grown considering texture coefficient of 1. In addition, texture coefficients for Mg_2Si (220) were only obtained in the heat treated samples (AB+HT, AB+HT+SP1 and AB+HT+SP2).

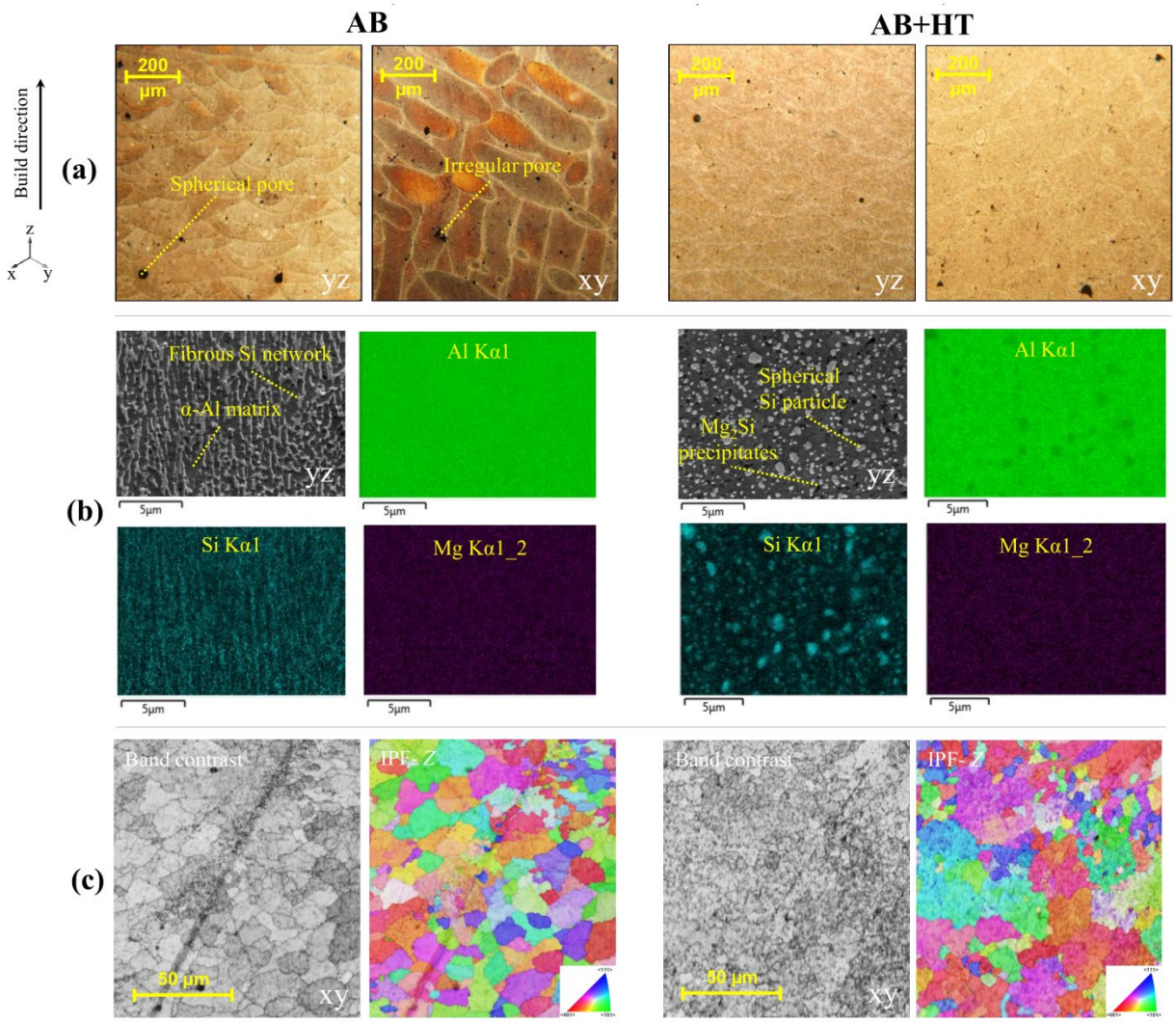

Fig. 3. Microstructural observations in AB (left) and AB+HT (right) samples (a) OM micrographs representing the microstructure of the AB and AB+HT samples in transversal and longitudinal cross-sections adopted from [58] (b) FESM observations of longitudinal and transversal cross-sections indicating the Si phase morphology and the corresponding EDS maps (c) Band contrast images and IPF-Z maps in transversal cross-sections for AB and AB+HT samples adopted from [58].

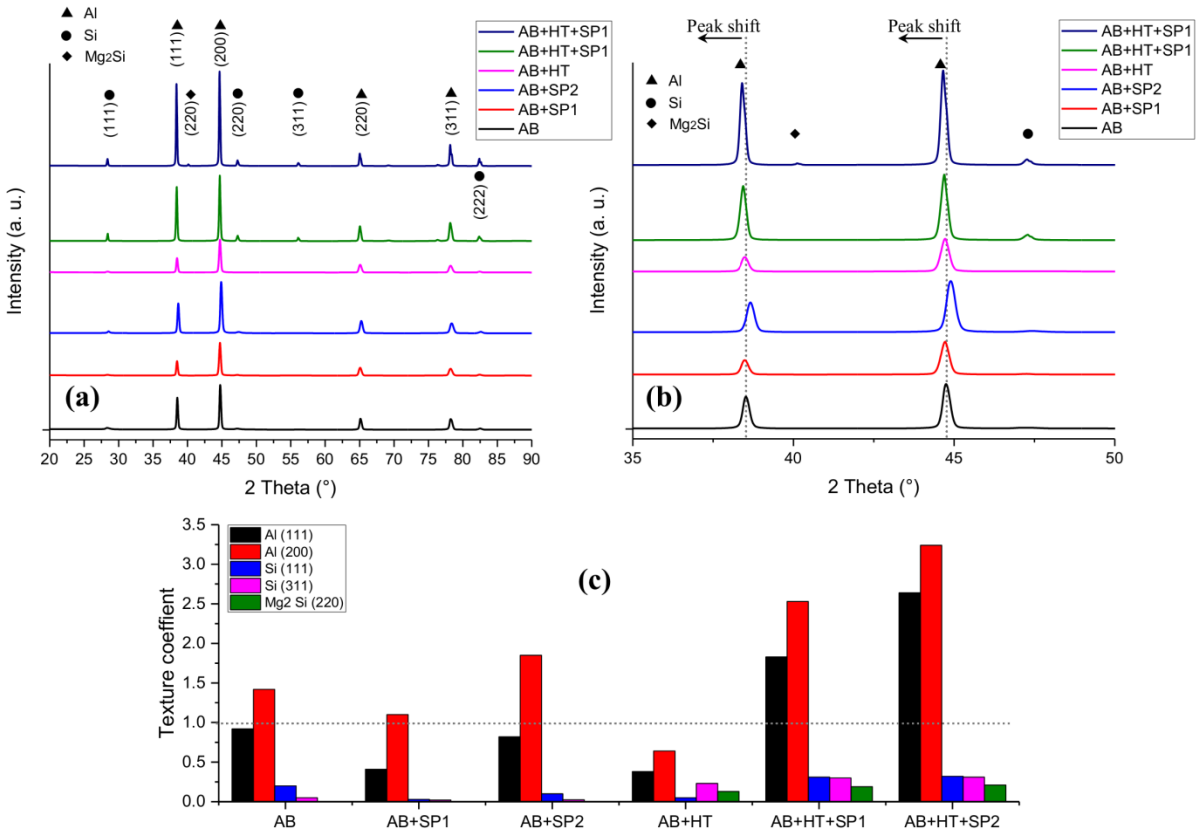

Fig. 4. XRD patterns of all samples along different diffraction angles of 2θ ranging between (a) 20-90° and (b) 35-50° (c) Texture coefficient analysis of all samples calculated from relative intensity values and X-ray diffraction peak data.

The results of different analyses of crystallographic orientation, grain boundary, recrystallization, Kernel average misorientation (KAM) and strain contouring performed by processing the EBSD results for the surface layer of the shot peened samples are shown in Fig. 5a and 5b. Transversal cross-section (*xy*-plane) along the building direction was conidered for all shot peened sets. IPF-*Z* maps reveal the random orientation of the grains in the surface layer compared to the dominant (001) orientation in the core material.

Grain boundaries with orientation of 2°< and 5°< were considered for processing. The grain boundary graphs, a higher density graind indicationg some extent of grain refinement could be observed near to the top surface of SP series. The observations confimred the presence of gradiant microstructures on SP series starting with ultrafine-grained (UFG) structure (< 0.5 µm) on the top surface layers gradually increasing to reach the original grain size at subsurface. SP1 treatment with higher intensity was found to be more effective regarding in-depth grain refinement on both AB and AB+HT series upto a depth of about 25 and 20 µm, respectively. SP2, on the other hand, showed thinner grain-refined layers with depths of about 12 and 7 µm on AB and AB+HT samples, respectively. It should be noted that both SP treatments were found to be more effective on AB samples rather than the AB+HT ones, due to the lower ductility and conformability of the material in AB condition.

Recrystalliazation graphs depict the distributions of recrystallized, substructured and deformed grains. In AB+SP2, AB+HT+SP1 and AB+HT+SP2 samples, deformed grains are mostly seen on the top surface layer upto the depth of about 15 µm; these samples have relatively high amounts of substructured grains and less scattered recrystallized grains. However, in the AB+SP1, due to the higher kinetic energy of the Applied SP treatment combined with the lower ductility of the base material in AB configuration, a very dense layer of highly deformed grians is generated on the top surface layer, which is gradually decresaded

through the ending part of the scanned area. In this sample, due to the presence of large number of deformed grians, the density of recrystallized and substructured grains are reduced considerably comapred to the other SP series.

KAM values can be used as an index of high plastic defrmation [79,80]. In all SP series, most concentrations are observed in the top surface layer with gradual reduction through the interior parts. The maximum KAM values were found in the regions with higher densities of refined grains.

Strain contouring maps can reflect the plastic strain variations of material after SP. The obtained strain contouring maps indicate that the strain increased from the bulk material to the shot peened surface. The strain values of the localized deformation for AB+SP1, AB+SP2, AB+HT+SP1 and AB+HT+SP2 samples are determined as 9.4, 6.4, 5.7 and 5.1 respectively. High grain refinment and surface layer hardening after SP lead to the increase of the plastic strain; as expected, the treatment with the highest intensity and kinetic energy (SP1) was the most efficient in inducing plastic strain. The variations of strain values are in agreement with the variations in the grain boundaries and misorientation distributions. In addition, it can be observed that the maximum values of strain were in the sub-surface and not exactly on the top treated surface, which is typicall for the surface plastically deformed materials [81,82]. Quantitative analysis of recrystallized, substructured and deformed grains are shown in Fig. 6a. Based on the EBSD results obtained within the scanned area of 32×10 μm^2, the average grain areas of 2.15, 0.56, 0.86, 5.5, 3.69 and 5.03 μm^2 were determined for AB, AB+SP1, AB+SP2, AB+HT, AB+HT+SP1 and AB+HT+SP2 samples, respectively (Fig. 6b). These results confirm grain size increase after heat treatment and the effect of SP in grain refienment. Similar trends were obtained for grain aspect ratio, which were decreased after SP (Fig. 6c).

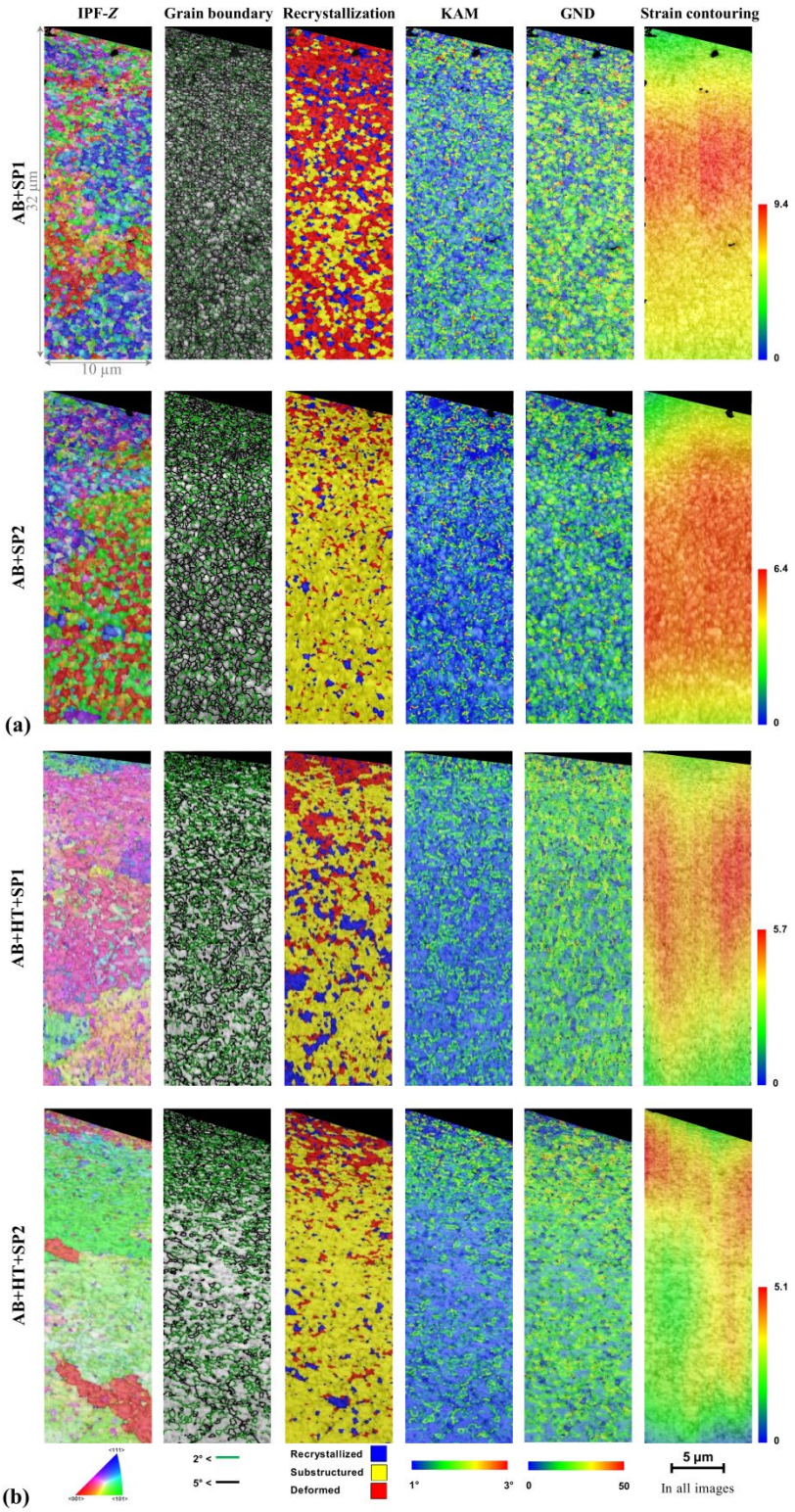

Fig. 5. EBSD analyses in terms of IPF-*Z*, grain boundary, dynamic recrystallization, KAM and strain contouring maps for (a) AB+SP series and (b) AB+HT+SP series.

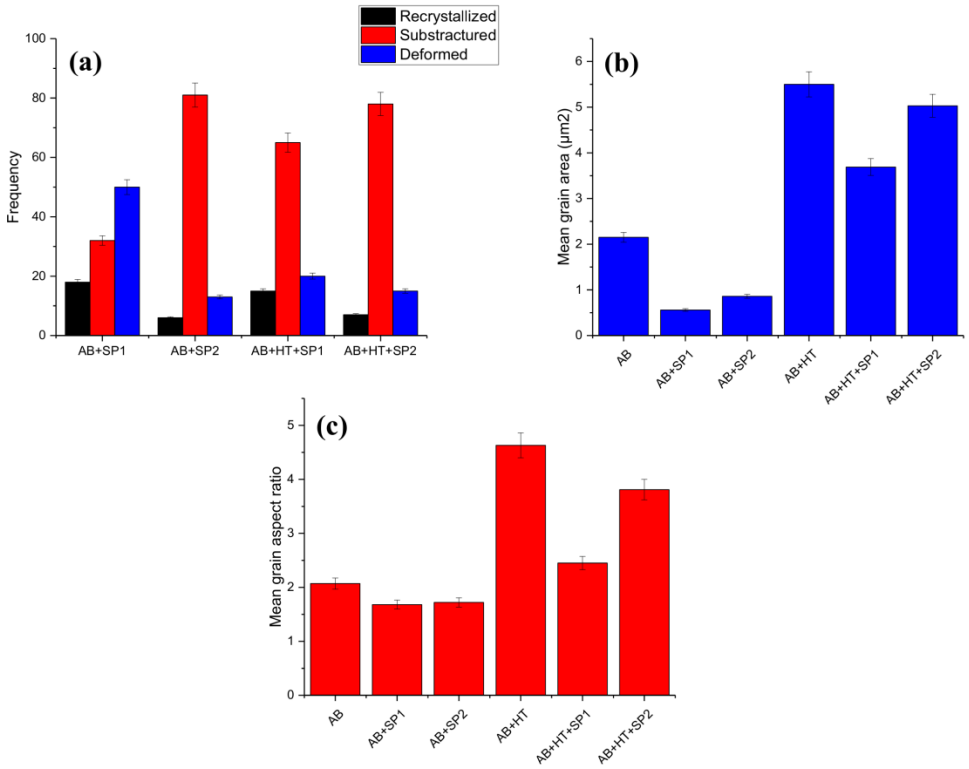

Fig. 6. Quantitative values of (a) recrystallized, substructured and deformed grains, (b) mean garin area and (c) mean grain aspect ratio.

Formation of columnar grains along the build direction in FCC metals [83] is reported to lead to the evolution of (001) fiber texture in AM state [84]. IPF-Z of samples presented in Fig. 7 clearly confirm the presence of (001) fiber textures in the both AB and AB+HT samples indicating that the applied heat treatment did not condierably affect the grain orientation, although it increase microstructural homogeneity. However, it can be seen that after SP, the grains are oriented in different random directions with different dominated texture orientations. For instance in AB+SP1 sample, (111) orientation is the dominated with strength of about 1.

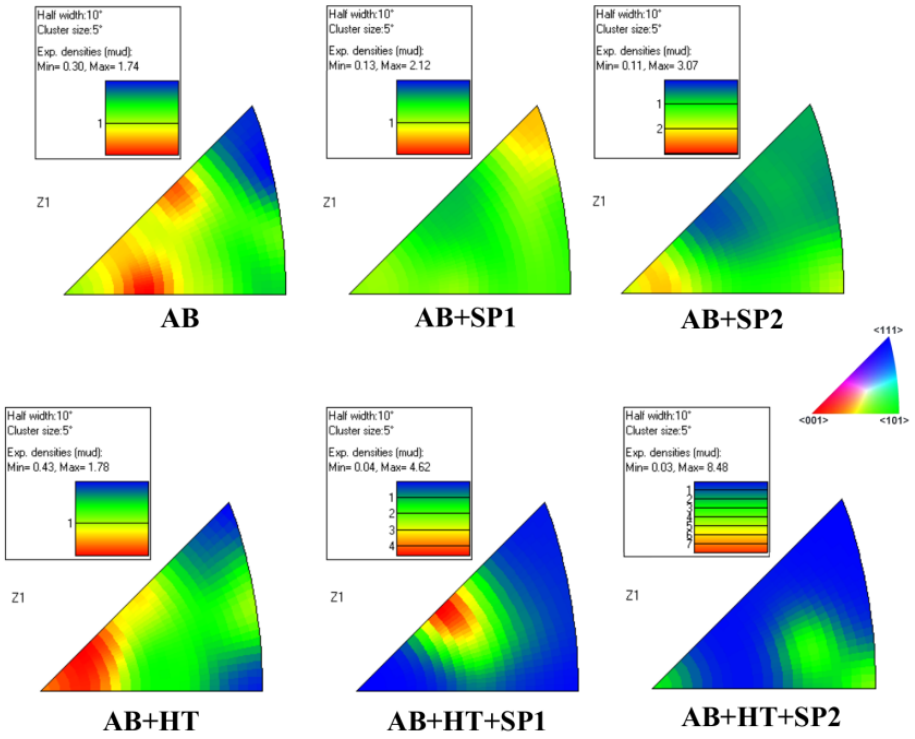

Fig. 7. Inverse pole figures (in *z*-direction) of as-built, heat-traed and shot peened samples.

3.3. Porosity analysis

The porosity measurements were carried out on all sets based on image analysis of BSE-SEM and OM micrographs in the notch area. The analysis was mainly focused on the internal and sub-surface porosities around the notch as presented in Fig. 8a and 8b, respectively. Similar trends were observed in the top and bottom areas with respect to the notch in all samples although the porosity in top surface was found to be slightly lower. The lowest porosity was detected in the mid area of the notch. OM observations near to the treated surface indicated that the SP treatments had no remarkable influence on the reduction of sub-surface porosities due to the low kinetic energy of the SP process parameters used in this study. However, as reported by Lesyk et al. [85], where higher SP parameters including intensity of 6-10C and peening duration of 60 s were used, pore closure and porosity reduction can be obtained. Porosity in the notched area was notably decreased after applying HT, which could be caused from cooling rate differences and different thermal histories. As reported by Bergant et al. [86] if suitable heat treatment is applied to AM material, the pores can be reduced and also most of the irregular pores can be transformed to spherical ones. Similar results are obtained in this study as presented in binarized micrographs of the AB and AB+HT samples in Fig. 8c.

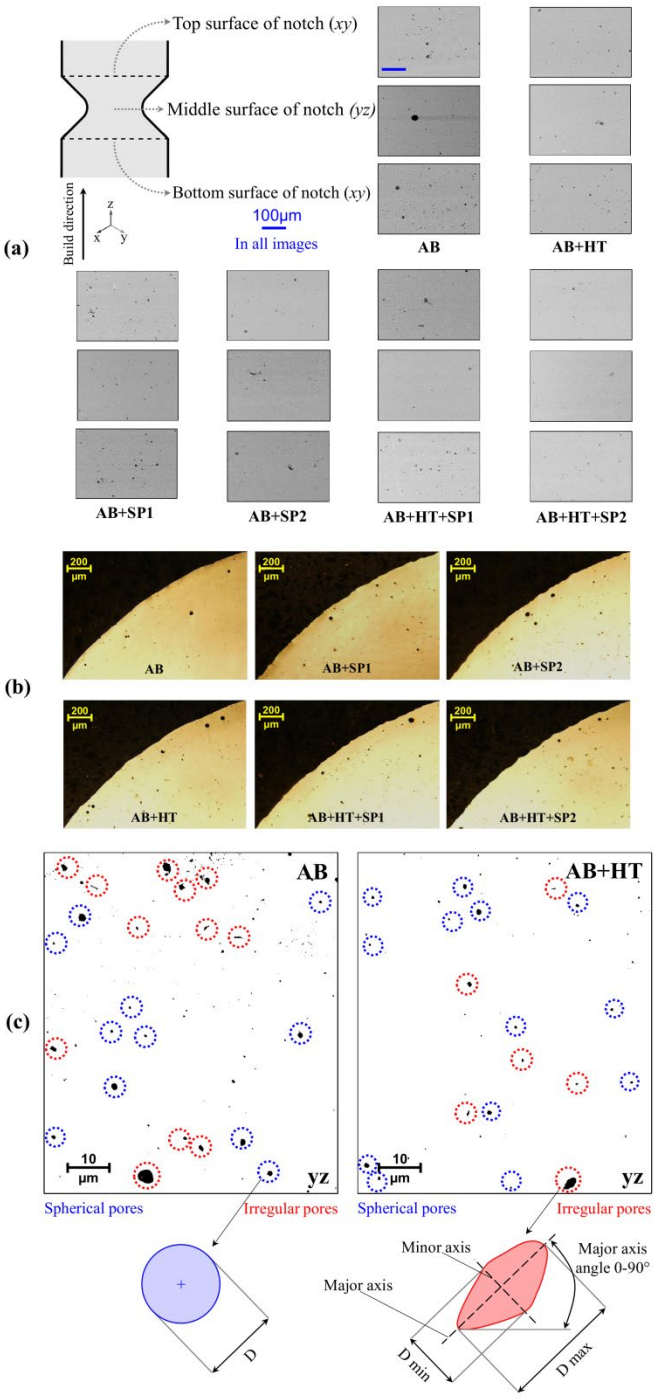

Fig. 8. (a) Schematic illustration of considered sections for image analysis and the selected zones in top, middle and bottom of the notch with corresponding BSE-SEM micrographs for all sets (b) OM observations of sub-surface porosities in all sets of samples adopted from [58] (c) Analysis of pore shape in terms of spherical and irregular pores in the AB and AB+HT samples using the binarized BS-SEM micrographs with the schematic illustration of the spherical and irregular pores' shape and dimension.

Quantitative image analysis results for porosity measurements illustrated in Fig. 9 indicate a porosity range of 0.40-0.48% for the inner parts of the samples in the notch root zone while in the sub-surface the porosities are slightly higher in the range of 0.51-0.56%.

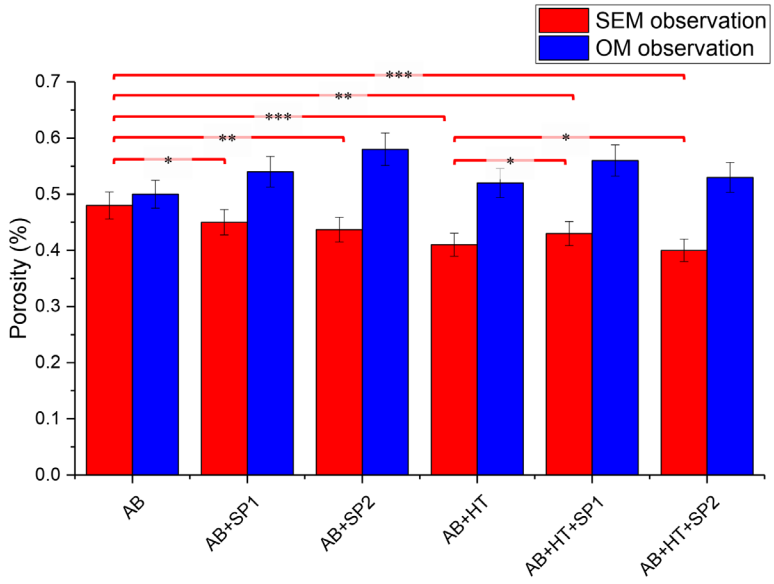

Fig. 9. Obtained results of porosity measurements using different methods for all sets of samples; *p < 0.05, **p < 0.01 and ***p < 0.001 obtained by statistical analysis.

3.4. Microhardness and residual stresses

Vickers microhardness tests were performed from the depth of 40 up to 740 µm in the transversal section of all sets as shown in Fig. 10a. The AB+HT series exhibit a remarkably reduced microhardness; AB and AB+HT samples showed hardness values of about 105 and 65 Hv, respectively. Similar trend for hardness reduction after thermal treatment was also reported in the study carried out by Zakay [87] on as-built and heat treated LPBF AlSi10Mg samples. However, after shot peening, the samples in both as-built and heat treated conditions represented a gradient profile of microhardness showing the maximum value on the top surface, which gradually decreased through the interior. As already discussed in the microstructural characterization section, the UFG microstructure and the grain refinement on the top surface layer induced by the plastic deformation caused by SP, will lead to increased hardening also based on the Hall-Petch relation. The depths of plastically deformed layer in shot peened samples (as-built and heat treated) were determined as 200 µm and 250 µm, respectively. Considering the initial hardness of AB and AB+HT samples, the top surface layer microhardness (measured at the depth 40 µm) in the shot peened series of AB+SP1, AB+SP2, AB+HT+SP1 and AB+HT+SP2 was enhanced up to about 15, 7, 20 and 6 %, respectively.

Residual stresses distributions were obtained by in-depth XRD analyses along a path perpendicular to the build direction as presented in Fig. 10a. In the AB sample, tensile residual stresses with a maximum of 31 MPa were determined. However, these tensile stresses were mostly relaxed after applying HT. In the shot peened samples, on-surface compressive stresses of −83 and -65 MPa, were continuously raised to reach a maximum value of −157 MPa at the depth of 180 µm and −170 MPa at the depth of 200 µm in AB+SP1 and AB+SP2 samples, respectively. The total depths affected by compressive stresses were measured as 530 µm and 480 µm for AB+SP1 and AB+SP2 samples, respectively. The total depth affected by compressive residual stresses was higher in the AB+SP1 sample in comparison with AB+SP2, caused by the higher Almen intensity of SP1 treatment.

On the other hand, in the heat treated condition although more compressive residual stresses are induced after relaxation of the tensile stresses, the results revealed lower surface residual stresses after applying SP

on heat treated samples. This can be attributed to the lower hardness and higher ductility of these sets as previously reported by Bagherifard *et al.* [51]. Similar to the AB condition, on-surface residual stresses of -46 and -31 MPa, increased to reach a peak value of -113 MPa at the depth of 400 µm and −103 MPa at the depth of 140 µm, respectively for HT+SP1 and HT+SP2 samples. However, affected depths by residual stresses are considerably increased up to 840 and 640 µm for HT+SP1 and HT+SP2 samples, respectively. The mechanical surface post-treatments were more efficient in terms of the maximum compressive residual stresses in AB series compared to the AB+HT ones, due to the initial different hardness [51]. The induced compressive residual stresses have major effects on improving the fatigue performance by the reduction of crack propagation rate.

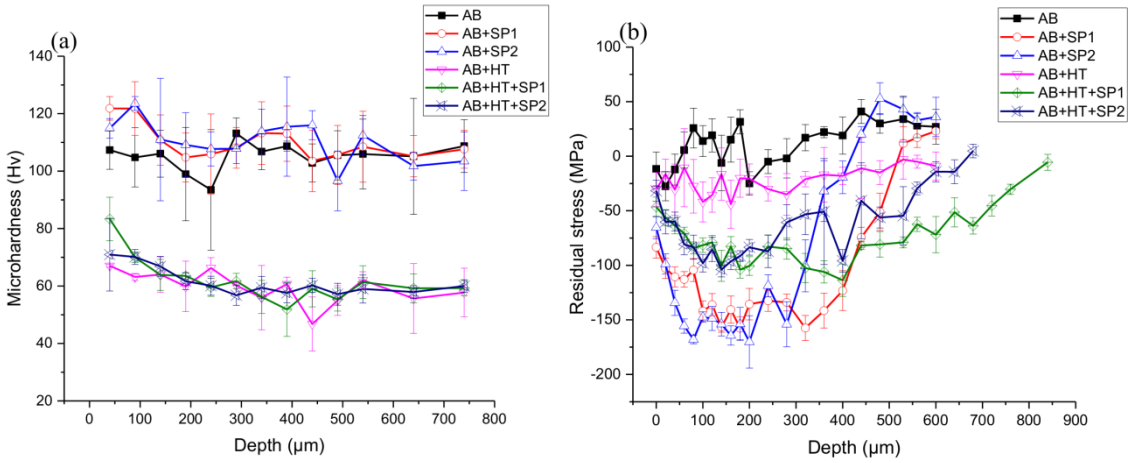

Fig. 10. (a) microhardness profiles and (b) distributions of determined residual stresses for all sets adopted from [58].

3.5. Surface morphology and roughness

Generally, LPBF materials have poor surface quality due to the formation of irregular surface features. In LPBF parts with complex geometries such as notches, which have downward and upward faces, more surface irregularities are observed especially in the downward surfaces, caused by the particular thermal history and the lower cooling rate [88]. Fig. 11a and 11b depict the surface morphologies of an AB sample in notch area and a smooth area, located 1 cm above the notch. In the smooth area, poor surface quality can be seen clearly. In the notch area, however, three distinct regions of upward face, notch root and downwards face can be identified with specific surface morphologies; the qualitative comparison shows the lowest surface quality for the downward face with a high density of surface irregularities followed by the notch root and then the upward face. Fig. 11c reveals different types of common surface defects including spatter, balling, unmelted and partially melted powders on downward face, which are specified based on the characteristics of surface imperfections in LPBF materials, categorized in the literature [6,89]. Spatters mainly form from ejection of liquid droplets from the melt pool due to the high power density of the reflected laser beam [90,91]. On the other hand, balling usually occurs after solidification of melt pool in the surface layer with discontinuity caused by the condensing oxide vapor on the liquid surface due to the high temperature gradient [92].

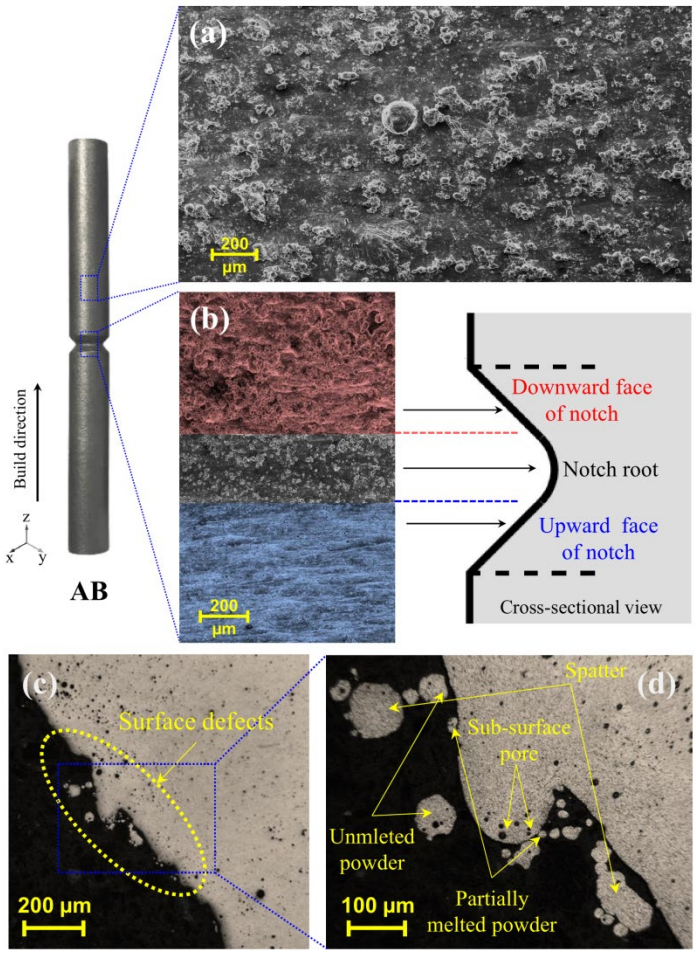

Fig. 11. Surface morphologies of LPBF AlSi10Mg in its as-built state in different regions of (a) smooth area and (b) notch area considering upward face of the notch, notch root and downwards face of the notch adopted from [58] (c,d) few representative surface defects specified in downward skin adopted from [58].

To modify the surface morphology and reduce the surface roughness, initially CP and ECP treatments were performed on the smooth area of AB samples, using 12 different parameter settings. The treated samples were screened in terms of qualitative analysis of surface morphology and quantitative effects on surface roughness reduction, and the best combination were applied on notched samples for further analysis. Fig. 12a and 12b represent the SEM observations of CP and ECP treated samples using different combinations of temperature or voltage and exposure times. It can be observed that by increasing time and temperature of CP, more regular surface morphologies were obtained with almost no signs of surface imperfections that were observed in the as-built condition. However, some oxidized areas and indications of pitting corrosion can be observed on the samples' surface, especially at higher exposure time. Similarly, in the ECP series, by increasing the time and voltage of the process, the efficiency of the treatment in inducing surface regularity became more notable.

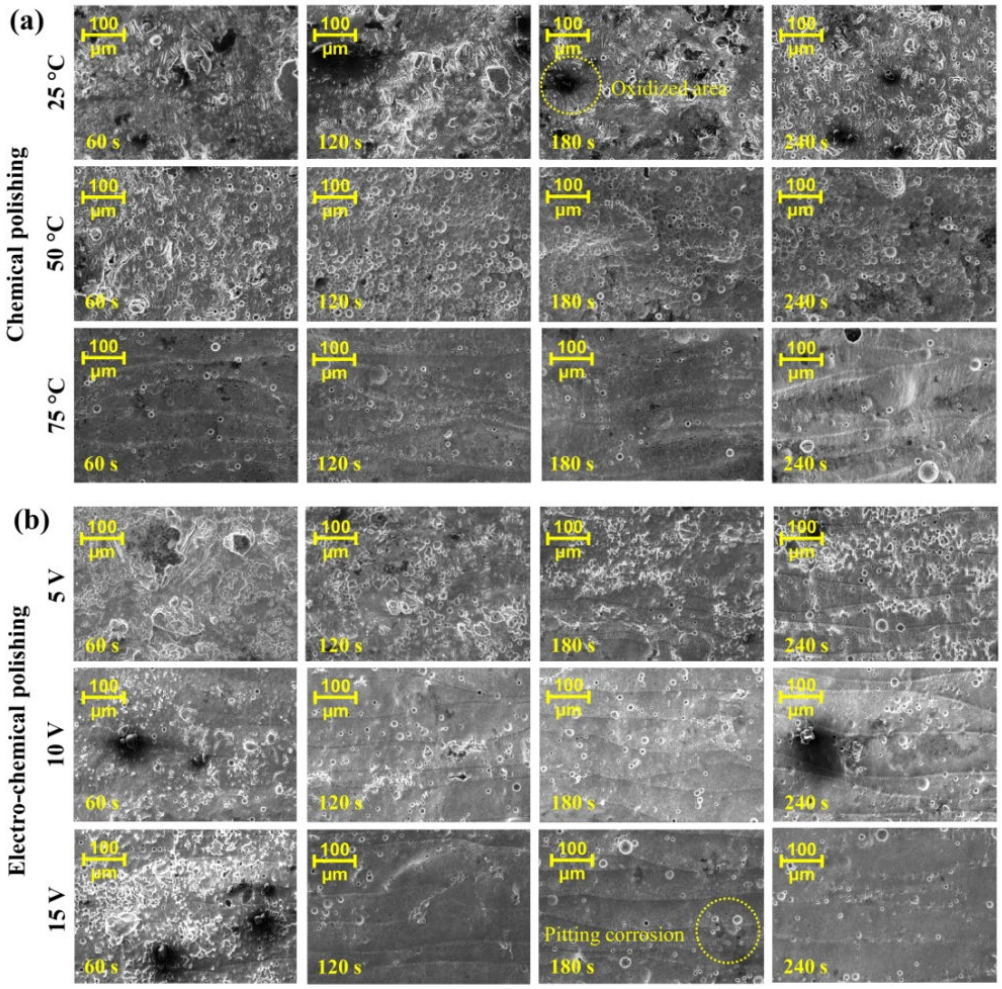

Fig. 12. The results obtained in the initial screening of chemical surface treatments with different process paramters for (a) CP and (b) ECP.

The obtained surface roughness parameters and mass loss are illustrated in Fig. 13a and 13b for CP and Fig. 13c and 13d for ECP samples, respectively; roughness values in terms of R_z, R_{zmax} and R_t are presented in Appendix A, for all measurements. Surface roughness was continuously reduced by simultaneous increasing of considered process parameters both for CP and ECP. The best combinations induced a roughness reduction of 4.49 µm in terms of R_a to 3.19 µm after CP with parameters of 75 °C and 240 s; the same initial R_a was reduced to 2.96 µm after ECP with a parameter combination of 15 V and 240 s. Therefore, these two chemical treatments were selected as optimum conditions of CP and ECP, respectively to be used for further analysis. These treatments correspond to mass loss of 8.65 and 1.87 % for the CP and ECP series, respectively. It was reported by Scherillo [33] that applying chemical brightening using a solution made of water, H_3PO_4,H_2SO_4, HNO_3, HF and $CuSO_4$ at 95°C for 7.5 min can reduce the surface roughness of LPBF AlSi10Mg up to 25% in the best scenario. Here, however, a further surface roughness reduction of 34% was obtained after applying ECP with 15 V and 240 s.

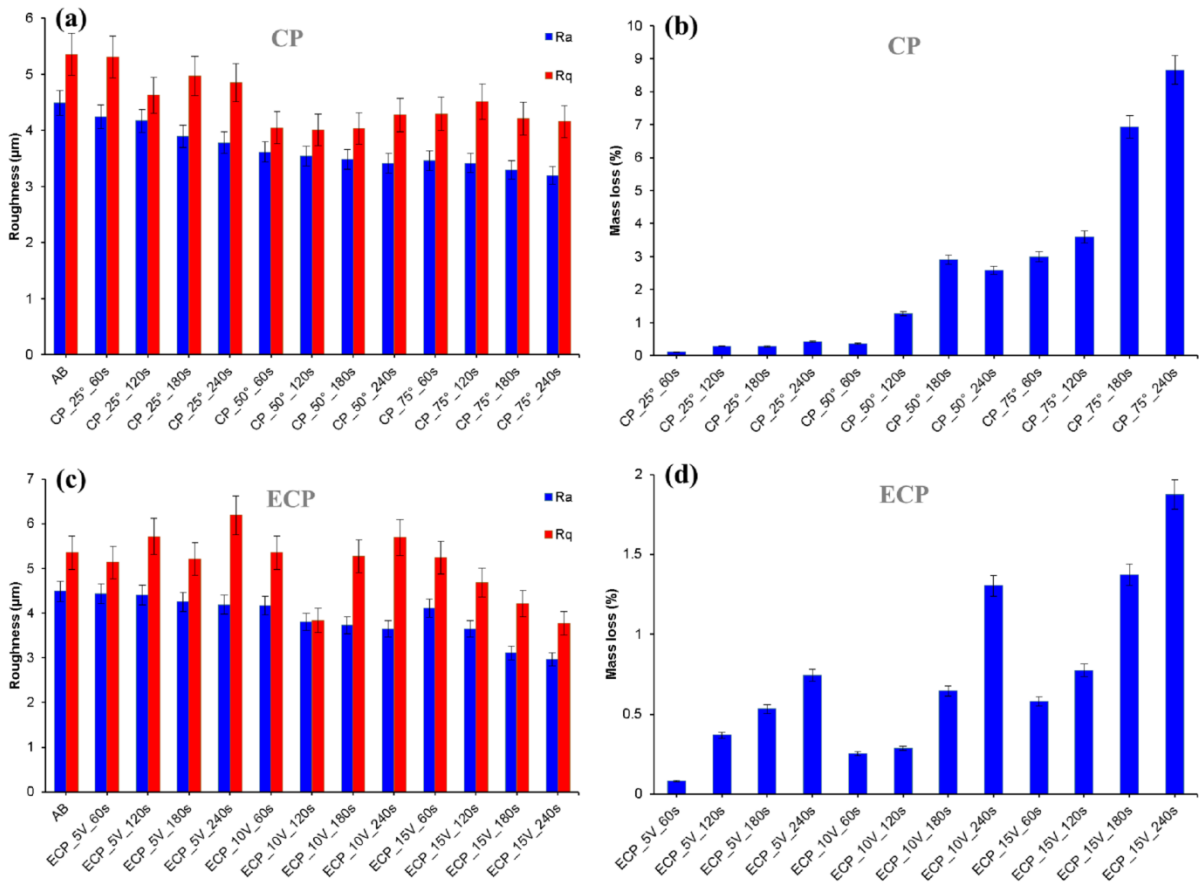

Fig. 13. Surface roughness paramters after applying (a) CP and (c) ECP treatments. The obtained mass loss of the chemically treated samples after (b) CP and (d) ECP treatments.

3.5. Fatigue behavior

The selected CP and ECP treatments were performed on AB notched samples to assess the contribution of these treatments to their fatigue behavior. Fig. 14a depicts the SEM micrographs taken from the notch area in AB, AB+CP and AB+ECP samples. The observations confirm that after CP, almost all the surface imperfections existed in the as-built state were eliminated; however, due to the high rate of corrosion, few new surface irregularities were formed on the surface of the material corresponding to the laser tracks. However, in the AB+ECP sample, many the surface defects were removed with no deep corrosion pits observed on the surface. In comparison with the effects of CP and ECP on the smooth area (Fig. 14a), the SEM observations at the notch area indicate that the efficiencies of the chemical treatments were decreased when applied on the notch area. 8.55 and 1.95 % mass loss were obtained for AB+CP and AB+ECP samples respectively considering initial mass of the samples (Fig. 14b). The diameter of the notch root in AB sample was reduced from 8.13 mm to 7.92 mm in AB+CP sample due to high degradation. On the other hand, after applying ECP as conformed by the low percentage of mass loss, the diameter of the notch root reduced to 8.03 mm, which is very close the as-designed dimension.

Rotating bending fatigue tests at fixed stress amplitude of 110 MPa were carried out on AB, AB+CP and AB+ECP series. Three samples were used for each set and the obtained fatigue lives are reported in Fig. 14c. The results indicate considerable fatigue life improvement after chemical treatments. Average fatigue life of AB sample with about 1.27×10^4 cycles, increased up to about 1.41×10^5 and 2.15×10^5 cycles in AB+CP and AB+ECP samples, respectively. The results indicate that among the two considered chemical treatments, ECP is more effective than CP in terms of fatigue life improvement of LPBF AlSi10Mg samples. Compared to the AB sample, the notch root diameter is reduced by 2.5 and 1.2% in AB+CP and

AB+ECP samples, respectively. The notch root diameter in the AB+CP sample is lower than the diameter in the as-designed geometry. This can result in further stress concentration in the notch area. In addition, AB+CP samples exhibited higher surface roughness compared to the AB+ECP series. Therefore, AB+ECP samples with lower surface roughness and less stress concentration in the notch root could reach higher fatigue life with respect to the AB+CP series. Hence, in the next step, the ECP treatment (15 V and 240 s) was applied to the heat treated and shot peened samples to also evaluate the effect of hybrid surface treatments on the fatigue performance of the samples.

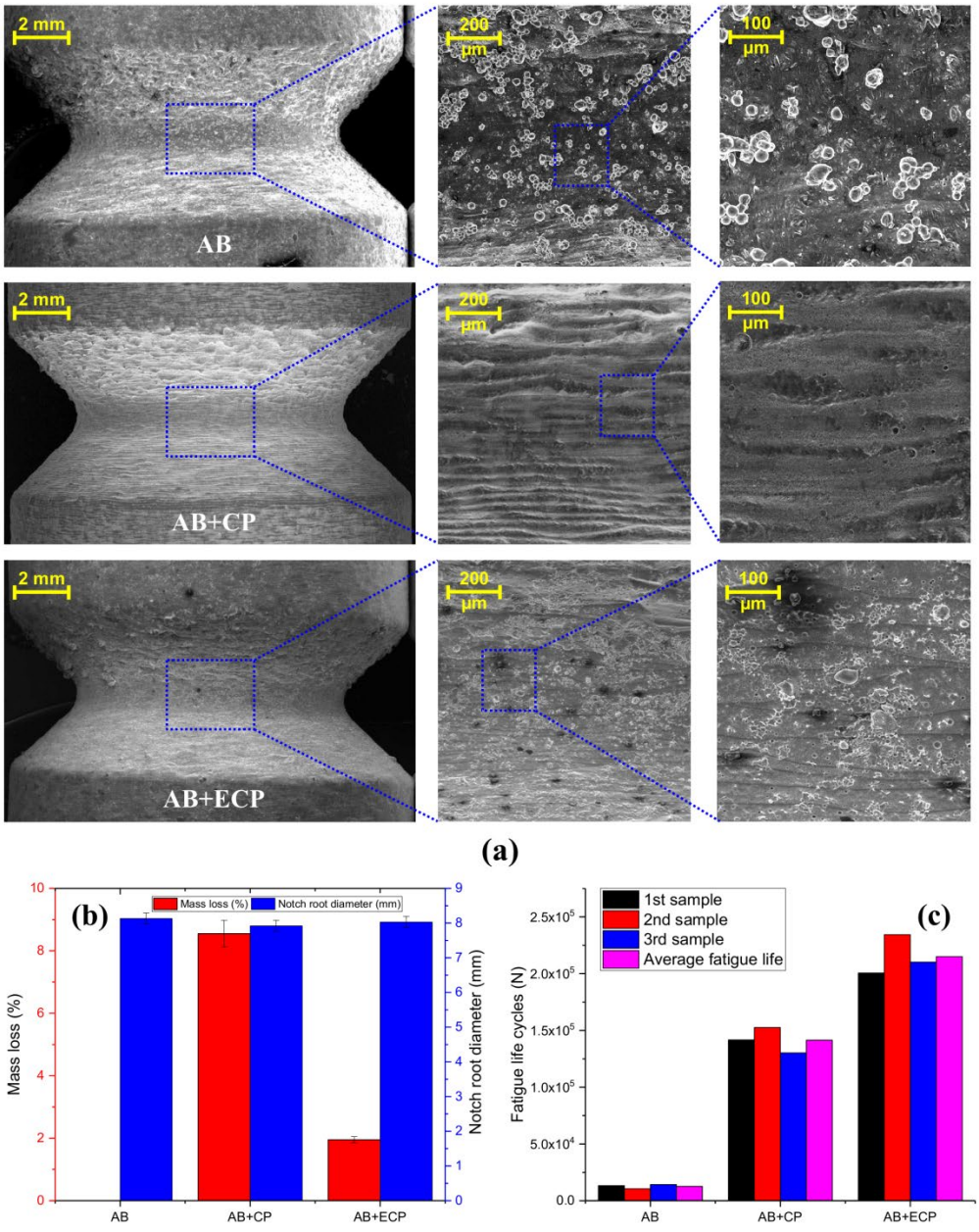

Fig. 14. (a) SEM observations of notch area in AB, AB+CP and AB+ECP samples (b) mass loss and notch root dimension of chemically treated samples (c) fatigue lives obatained at amplitude stress of 110 MPa for AB, AB+CP and AB+ECP series.

Fig. 15a represents the initial states of surface morphologies of shot peened sample as well as the heat treated one in the cylindrical part of the samples. Considering AB and AB+HT seriess (HT has no effect on surface morphology variation) with very high surface irregularties, it can be observed that in the shot peened samples surface imperfections and irregularities are remarkably reduced and the surface morphologies are highly modifed to become more regular compared to the initial AB state. Surface morphology modification of LPBF AlSi10Mg after applying SP was also investigated by Uzan et al. [17]. They utilized steel shots of S110 with Almen intensity 5 A [0.001 inch] at a surface coverage of 100%. In addition, comparing the effects of the two applied SP treatments (SP1 and SP2) reveals that SP2 has higher influnce on surface modification by forming more regular surfaces. These results indiacte that with respect to the same coverage of 100%, smaller impacting media of SP with higher hardness (ceramic shot) can be more effective for surface morphology modification compared to the larger shot with lower hardness (steel shot), even if it has lower Almen intensity.

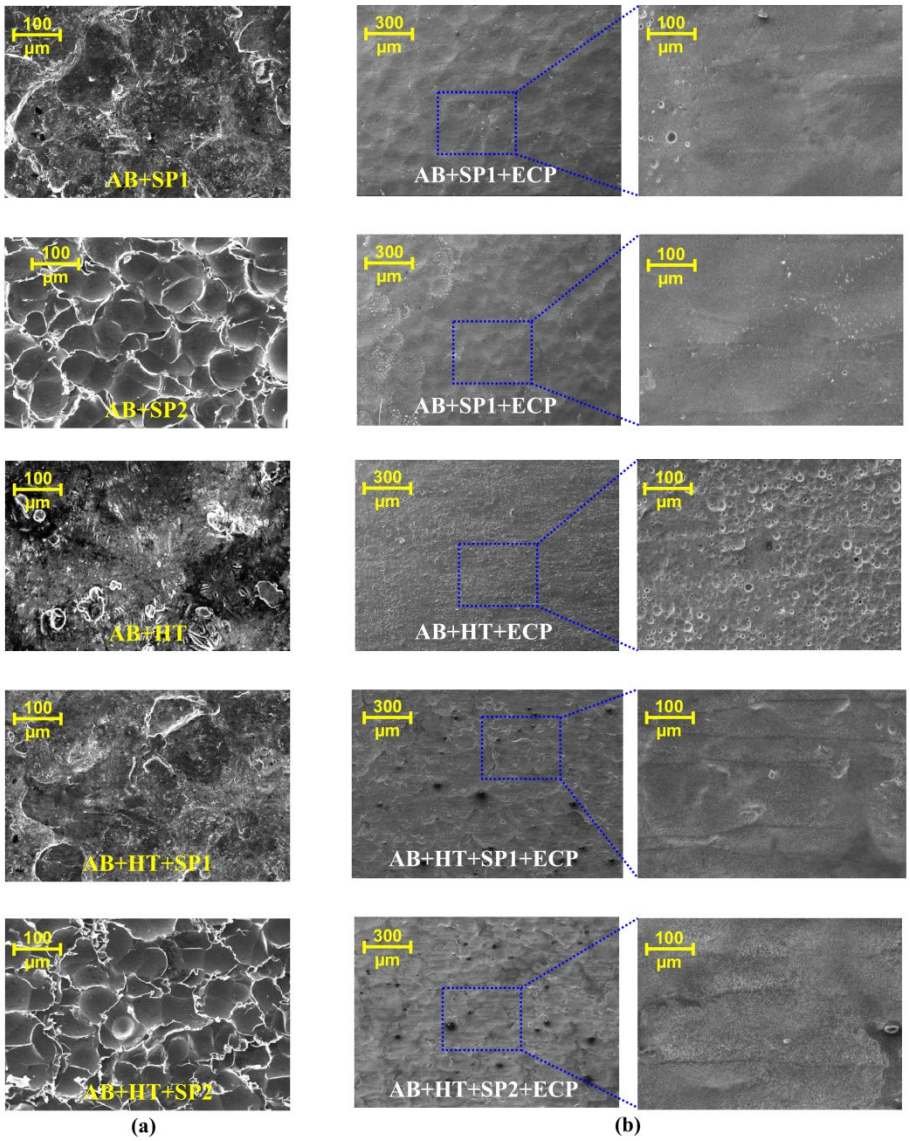

Fig. 15. SEM micrographs of shot peened and heat treated samples' surfaces (a) before and (b) after applying ECP.

Fig. 15b presents the SEM surface morphologies of the samples initially heat treated and shot peened samples after applying hybrid treatments with the final step of ECP. The results indicate high efficiency of ECP on modifying the surface morphologies. The previously formed dimples caused by the shot impacts were almost completely removed through the application of the chemical treatment. In addition, in both AB and AB+HT samples, the traces of pitting corrosions could be observed in some parts. However, in the shot peened samples, the higher surface hardness led to a higher resistance to pitting corrosions [93]; these samples also exhibited a more homogenous surface morphology almost free from the surface defects.

Fig. 16a represents the surface roughness parameters for all treated samples and compares them with the initial as-built state. Considering the effects of single step treatments, the AB and AB+HT samples represented the identical surface roughness of 4.48 µm and 4.43 µm, respectively in terms of R_a, both were reduced after ECP to 2.96 µm and increased after SP1 and SP2 to 4.61 and 8.60 µm, respectively. SP2 which uses harder and smaller shots enhanced the roughness more than SP1, despite its lower Almen intensity.

In the hybrid treatments obtained by combination of HT and SP, the microstructural homogenization and improved ductility after the heat treatment, led to the formation of deeper dimples by the impacting shots during SP. Hence, AB+HT+SP1 and AB+HT+SP2 samples showed slightly higher surface roughness of 6.67 and 8.91 µm in terms of R_a respectively, compared to the not heat treated counterparts.

Contrastingly, due to the material removal nature of ECP, the samples subjected to hybrid treatments with the final step of ECP showed considerable roughness reduction representing R_a values of 3.29, 3.44, 2.61, 4.12 and 4.21 µm for AB+SP1+ECP, AB+SP2+ECP, AB+HT+ECP, AB+HT+SP1+ECP and AB+HT+SP2+ECP samples, respectively. The final material removal step was able to reduce the surface roughness compared to the as-built condition in the AB+SP2 and AB+HT+SP2 samples, which had relatively high surface roughness before chemical treatment.

Fig. 16b depicts the measured mass loss after applying ECP on heat treated and shot peened samples. AB+HT+ECP and AB+ECP with 1.85 and 1.95 % show the highest mass loss among the considered samples. The heat treated samples, on the other hand, show lower rate of material removal due to their different material properties.

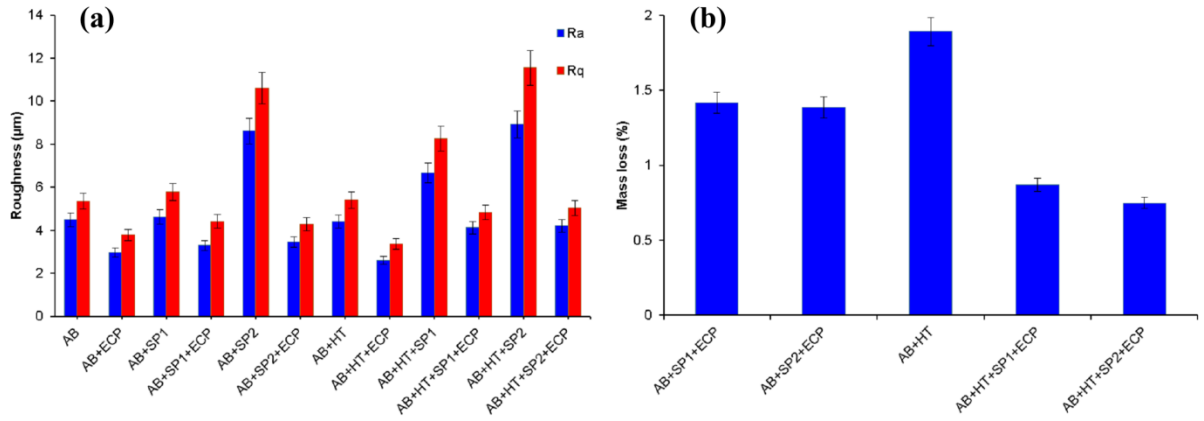

Fig. 16. Surface roughness for as-built and surface treated samples including also the hybrid treatments (d) mass loss after applying ECP on shot peened and heat treated samples.

Fig. 17 illustrates the SEM micrographs of notch area before and after applying ECP on samples treated by SP, HT and their combinations. Application of ECP mostly removed the dimples generated by SP treatments leading to a homogenous surface with relatively low roughness, especially in AB+HT+SP1+ECP and AB+HT+SP2+ECP samples. Also, in AB+HT sample, the initial surface irregularities such as partially melted and unmelted powders were mainly removed.

Fig. 18a reveals the measured notch root diameter and mass loss of the samples after performing HT, SP1, SP2, ECP and their combinations on notched fatigue samples. It can be seen that due to the low rate

of material removal (maximum of 1.95% for AB+ECP) after ECP, the notch root diameters were reduced to around 8 mm in all samples but not lower. The results of the fatigue tests performed at a stress level of 110 MPa are shown in Fig. 18b and the average fatigue lives and the corresponding fatigue life improvements are presented in Table 3. The results indicate notable fatigue behavior improvements after applying hybrid post-treatments including HT, SP and ECP together. The effect of sequential application of the post-treatments can be analyzed by comparing the average fatigue life of AB sample that is improved up to 2, 23 and 44 times in AB+HT, AB+HT+SP2 and AB+HT+SP2+ECP samples, respectively.

Each of the applied treatments has a distinct contribution to the fatigue life improvement. HT improves the fatigue life through microstructural homogenization and increasing ductility. SP contributes by three major effects including surface layer grain refinement and hardening, inducing considerable compressive residual stresses and also modifying the surface morphology to a more homogenous state. Furthermore, ECP enhances the fatigue life due to the remarkable roughness reduction and altering the surface morphology to a smoother surface with almost no imperfections. Dealing with single treatments, SP (SP2 more than SP1) has the highest performance followed by ECP and HT on average fatigue life improvement. Accordingly, a hybrid treatment with the sequential application of HT, SP and ECP, can exploit all the positive effects simultaneously and highly improve the fatigue life of AM samples with irregular geometries.

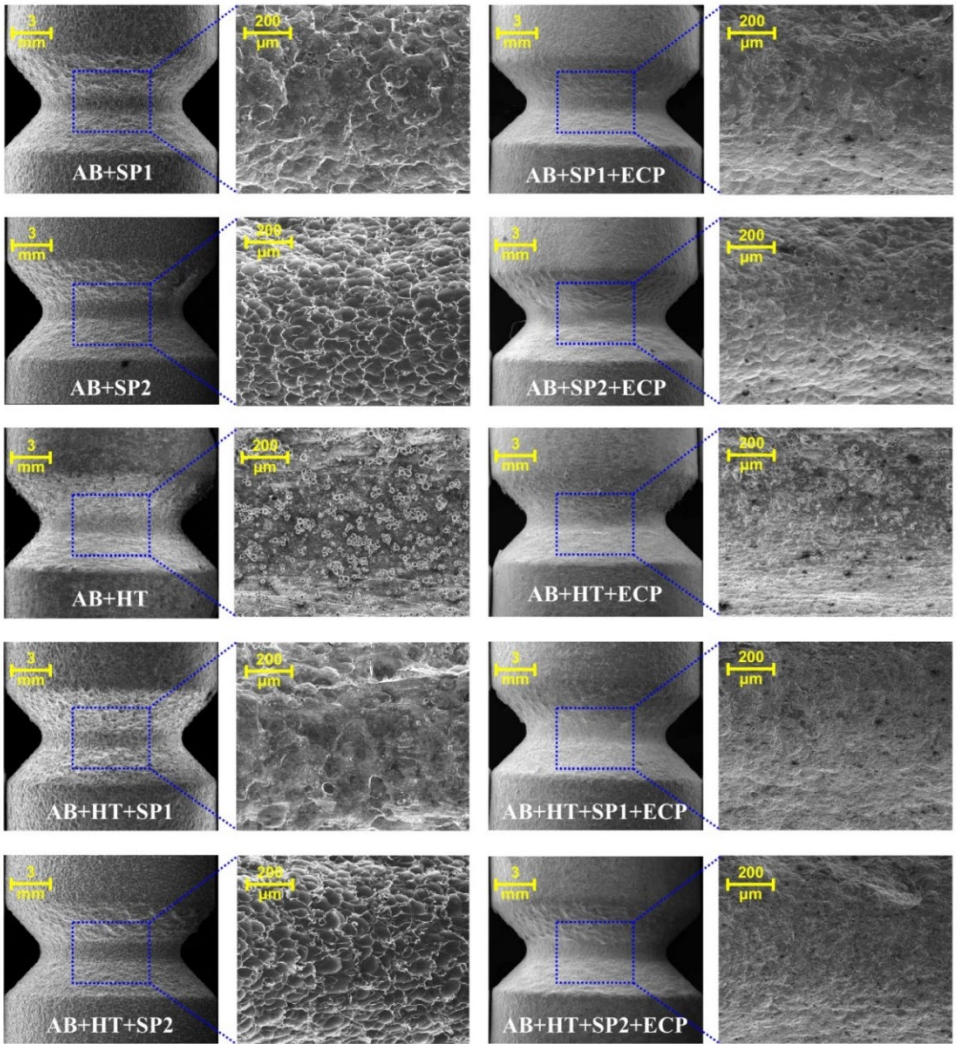

Fig. 17. SEM micrographs showing the surface morphology of the notch area for surface samples treated with HT, SP1, SP2, ECP and their combinations.

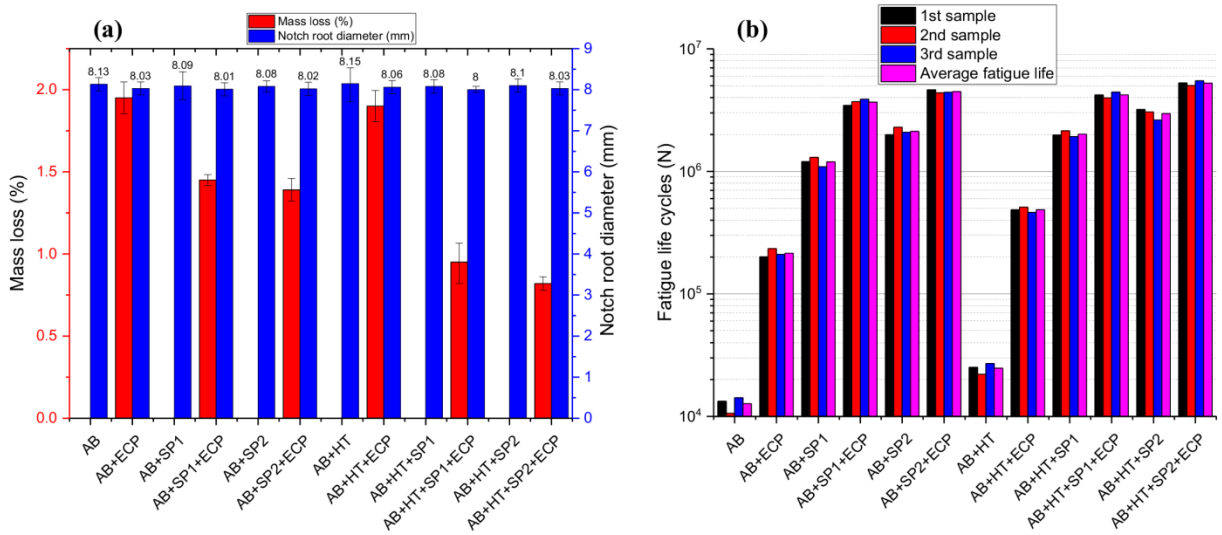

Fig. 18. (a) measured mass loss and notch radius diameter before and after applying ECP (b) fatigue lives obtained at the amplitude stress of 110 MPa for AB and post-treated samples.

Table 3. Average fatigue lives and the corresponding fatigue life improvements for post-treated samples compared to the as-built state

Sample ID	**Average fatigue life (cycles)**	**Fatigue life improvement compared to as-built state (times higher)**
AB	1.26×10^4	1
AB+ECP	2.15×10^5	17
AB+SP1	1.19×10^6	94
AB+SP1+ECP	3.67×10^6	290
AB+SP2	2.11×10^6	167
AB+SP2+ECP	4.47×10^6	353
AB+HT	2.47×10^4	2
AB+HT+ECP	4.86×10^5	38
AB+HT+SP1	2.01×10^6	159
AB+HT+SP1+ECP	4.20×10^6	331
AB+HT+SP2	2.95×10^6	233
AB+HT+SP2+ECP	5.25×10^6	414

Recent studies have revealed that although theoretically the notch root accounts for the highest stress concentration in the component, it is not always the fatigue failure site. Fatigue fracture has been reported to mainly initiate on the downward face of notch due to the high surface roughness and the presence of potential crack nucleation sites [94]. Parameter of relative height (h/h_0) defines the locations of fracture sites that can be calculated as the ratio of distance of the failure initiation site from the notch root (h) to the total notch opening (h_0).

The relative height of failure site was calculated for all sets as an average of 15 measurements per each set. The h_0 *value* was considered as 4.8 µm for all samples as extracted from the initial design. Fig. 19a presents the variations of the fracture surface location in different treated sets compared to the AB (with $h=h_{AB}$) and AB+HT (with $h=h_{AB+HT}$). The schematic illustration of failure site definition and the determined results in terms of relative height of notch for all sets in the same notch acuity of $\xi=0.3$ are depicted in Fig. 19b. The results indicate that, the post-treatments clearly alter the location of fracture site and shift it closer to the notch root direction. Considering the sole effects of applied post-treatments, SP2, ECP, HT and SP1 have the highest efficiency in shifting the fracture site closer to the notch root, respectively. The hybrid

treatments are even more effective with the AB+HT+SP2+ECP sample representing the smallest distance between the fracture site and the notch root.

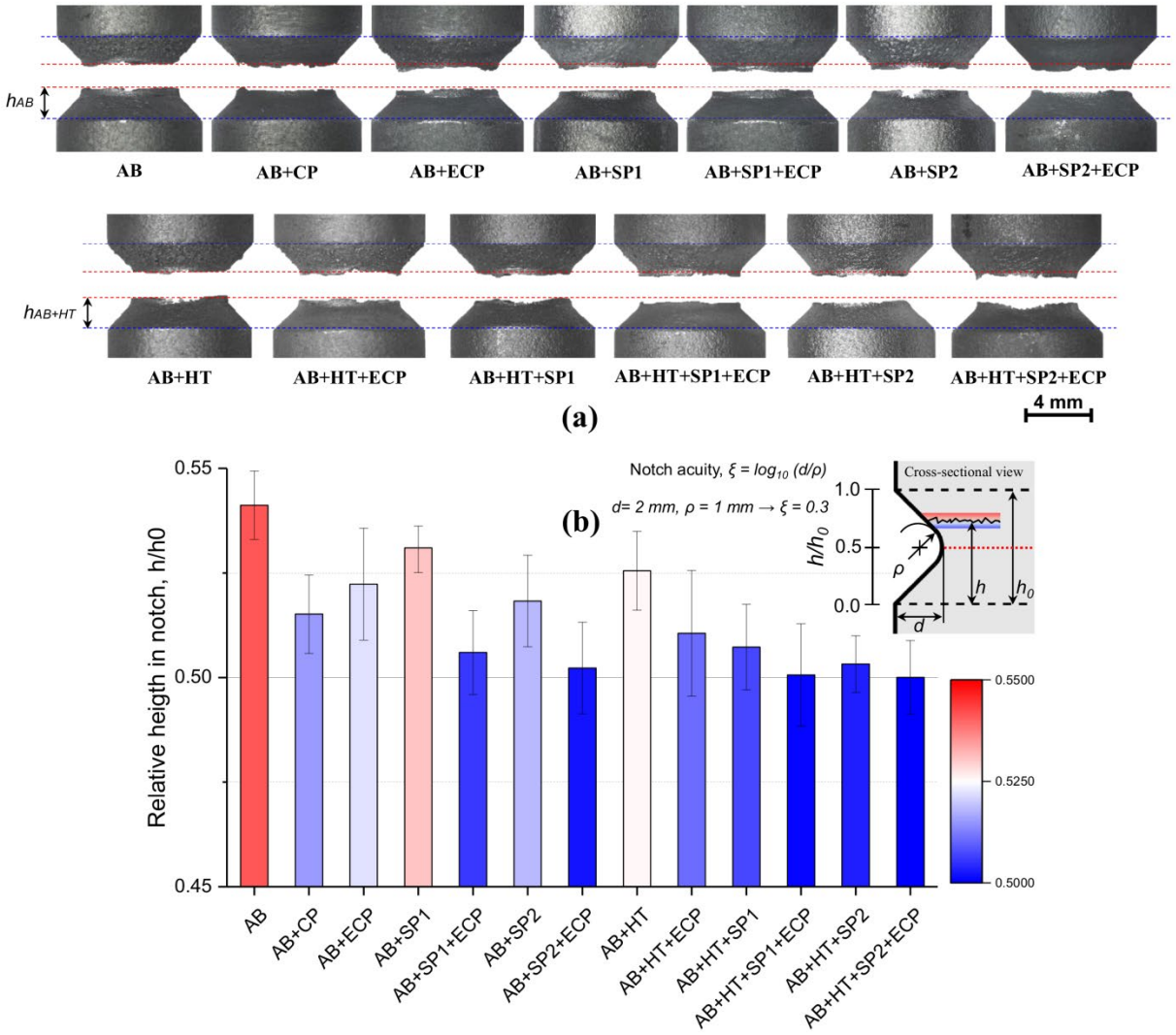

Fig. 19. (a) Stereo-OM observations of fracture sites in all sets (b) schematic illustration of failure site definition and the obtained results in terms of relative height of notch in the as-built and post-treated samples.

The applied post-treatments changed the microstructural, surface and mechanical properties as well as the fatigue behavior. Sole effects of each post-treatment on microstructural characteristic, ductility, hardness, residual stresses, surface morphology, roughness and fatigue behavior are summarized in Fig. 20. It can be observed that, all the considered treatments led to fatigue life improvement. SP2 and SP1 have almost similar contributions on hardening and inducing compressive residual stresses. The AB+SP2 sample reached to the higher fatigue life despite its higher roughness compared to AB+SP1 series; this could be caused by its more homogenous surface morphology compared to the AB+SP1 samples. These results indicate that besides the surface roughness reduction (which can be obtained by ECP), surface morphology (that can be described by roughness parameters) has considerable influence on fatigue behavior of the notched samples. Therefore, as expected applying hybrid treatment, which includes both these beneficial features leads to a more remarkable fatigue life improvement (as obtained for AB+HT+SP2+ECP sample).

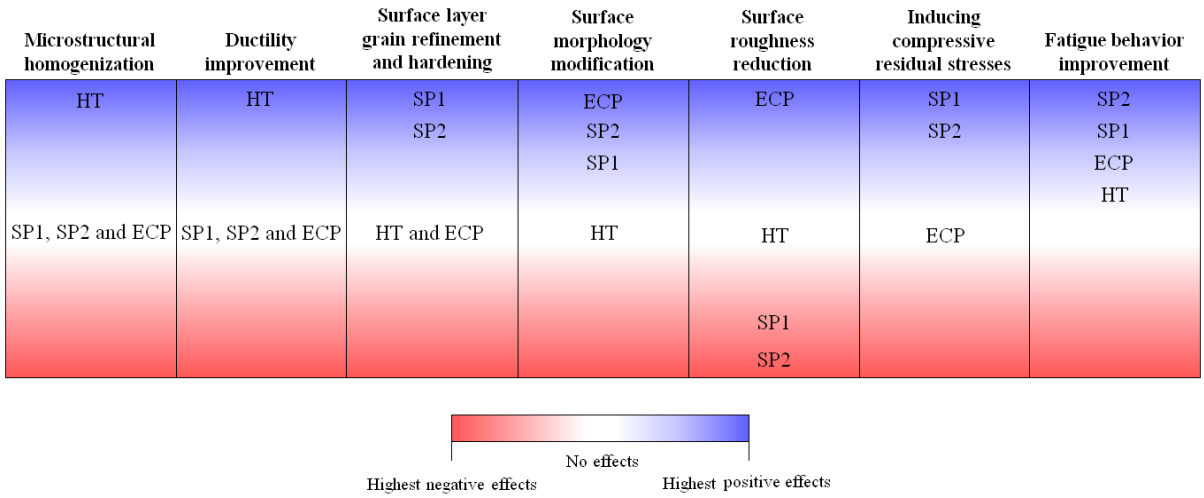

Fig. 20. An overall comparison of the sole effects of each post-treatment on microstructural and mechanical characteristic compared to the as-built state (HT not placed in the CRS column as it is more relaxing the tensile stresses rather than inducing CRS).

Besides improving the mechanical performance of the LPBF material, producing the final part in an economic manner is also quite substantial. Two different analyses including sole cost (money-time) analysis and cost-performance analysis were performed. In these analyses, time, costs, and especially performance of the effect of post-treatment on fatigue life improvement were considered as the key variable parameters. Each parameter was rated into five comparative levels of very low, low, moderate, high and very high. Scores of 1-5 were assigned to each level for developing a semi-quantitative matrix according to the common approach used in cost and risk analysis [95,96]. A symmetric distribution was considered for the cells assigned to related level for the considered parameters in this matrix, as a practical tool for analysing the relevant ranks [97]. The constructed matrixes of cost-time and cost-performance analyses are presented in Fig. 21a and 21b, respectively. Fig. 21c represents the assigned scores to each post-treatment and the obtained final score and ranks. The comparative levels of time and costs corresponding to each parameter were estimated based on the authors' experience. The levels of performance were assigned based on the experimental fatigue test results. The obtained scores of money-time analysis were used as cost parameter in the cost-performance analysis. Considering both economical and fatigue improvement factors, it can be observed that applying sole SP can be the best option with first rank followed by ECP and hybrid treatment of HT+SP+ECP in the second and third ranks, respectively. The hybrid treatment of SP+ECP commonly had the fourth rank.

It should be mentioned that the presented results in this part are to compare the performance of the applied treatments only in economic terms, regardless their eventual contribution to fatigue performance. However, as it was mentioned before, the single treatments of SP, ECP and HT have the highest performance on average fatigue life improvement, respectively.

(a)

Time-money analysis matrix						
Time	Very High	5	5	10	15	20	25
	High	4	4	8	12	16	20
	Moderate	3	3	6	9	12	15
	Low	2	2	4	6	8	10
	Very Low	1	1	2	3	4	5
			1	2	3	4	5
			Very Low	Low	Moderate	High	Very High
			Money				

Ideal	Moderate	Not-ideal

(b)

Cost-performance analysis matrix						
Cost	Very High	5	5	10	15	20	25
	High	4	4	8	12	16	20
	Moderate	3	3	6	9	12	15
	Low	2	2	4	6	8	10
	Very Low	1	1	2	3	4	5
			1	2	3	4	5
			Very High	High	Moderate	Low	Very Low
			Performance				

Ideal	Moderate	Not-ideal

(c)

Post-treatment	Time-money				Cost-performance			
	Time	Money	Final Score	Rank	Cost	Performance	Final Score	Rank
HT	Moderate	Low	6	3	Low	Very low	10	7
SP	Low	Low	4	2	Very low	Moderate	3	1
ECP	Very low	Very low	1	1	Very low	Low	4	2
HT+SP	High	High	16	5	High	High	8	5
HT+ECP	High	Moderate	12	4	Moderate	Moderate	9	6
SP+ECP	Moderate	High	12	4	Moderate	High	6	4
HT+SP+ECP	Very high	Very High	25	6	Very high	Very high	5	3

Fig. 21. Rating of the variable parameters considering five different levels and the corresponding scores for (a cost and (b) cost-performance analyses. (C) Scores and ranks of the applied post-treatments in terms of cost and cost-performance analyses.

4. Conclusion

LPBF materials show numerous imperfections in terms of microstructure and surface quality in the as-built state; these could lead deteriorate mechanical performance especially regarding fatigue behaviour. Post-treatments can play substantial role to overcome these defects. In the present study, the effects of four different post-treatments including heat treatment, mechanical surface treatment and chemical surface treatment as well as their combination as hybrid treatments were investigated on microstructural and mechanical properties of LPBF V-notched AlSi10Mg samples. The effects of heat treatment, two different shot peening treatments (with different Almen intensity, shot diameter and shot hardness) as well as two processes of chemical polishing and electro-chemical polishing were studied, through experimental analyses. Based on the obtained results the following conclusions can be drawn:

- The surface morphology imperfections were more notable on the downward skin of the notch.
- Inhomogeneous microstructure observed in the as-built state was considerably modified after the heat treatment. This modification improved the ductility of the material up to 5 times. Furthermore, the tensile residual stresses were relaxed after heat treatment.
- Surface layer grain refinement was obtained by shot peening treatments. This led to increased microhardness on the top surface up to 13%. Considerable compressive residual stresses were induced in the surface layer up to about -175 MPa with a corresponding depth of 200 µm.
- Microhardness and residual stress measurements on shot peened samples revealed that the higher Almen intensity led to higher surface hardness (122 vs. 117 Hv after shot peening treatment with steel and ceramic shots, respectively) and higher on-surface compressive residual stresses (-83 vs. -65 MPa after shot peening treatment with steel and ceramic shots, respectively).

- Shot peening increased the surface roughness; however, it had a significant effect on homogenising the surface morphology and obtaining more regular surfaces.
- Ceramic shots with smaller diameter and higher hardness compared to the larger steel shots were more efficient in modifying the surface morphology (8.60 μm after shot peening with ceramic shots and 4.61 μm for shot peening with the steel shots vs. 4.48 μm for the as-built condition in terms of Ra).
- Chemical treatments efficiently removed the surface irregularities of the as-built material and reduced the surface roughness from 4.48 μm to 3.19 and 2.97 μm in terms of Ra after chemical and electro-chemical polishing, respectively.
- Fatigue life was increased up to about 17 and 11 times after electrochemical and chemical polishing, respectively.
- All the applied post-treatments enhanced the fatigue performance of the notched samples. Considering single post-treatments, shot peening with ceramic shot was found to be the most efficient followed by electro-chemical polishing and heat treatment with life cycles increased up to 167, 17 and 2 times higher than as-built condition, respectively.
- The hybrid treatments led to additional fatigue life improvement. Combination of heat treatment + shot peening with ceramic shots + electro-chemical polishing had the highest effects on fatigue life improvement leading to 414 times higher fatigue life compared to the as-built state.
- Considering the cost-performance analyses with respect to the time, money and performance, to obtain the highest fatigue efficiency in the V-notched AlSi10Mg samples in an economical manner, shot peening can be the best option ranked first followed by electro-chemical polishing in the second rank.

Appendix A

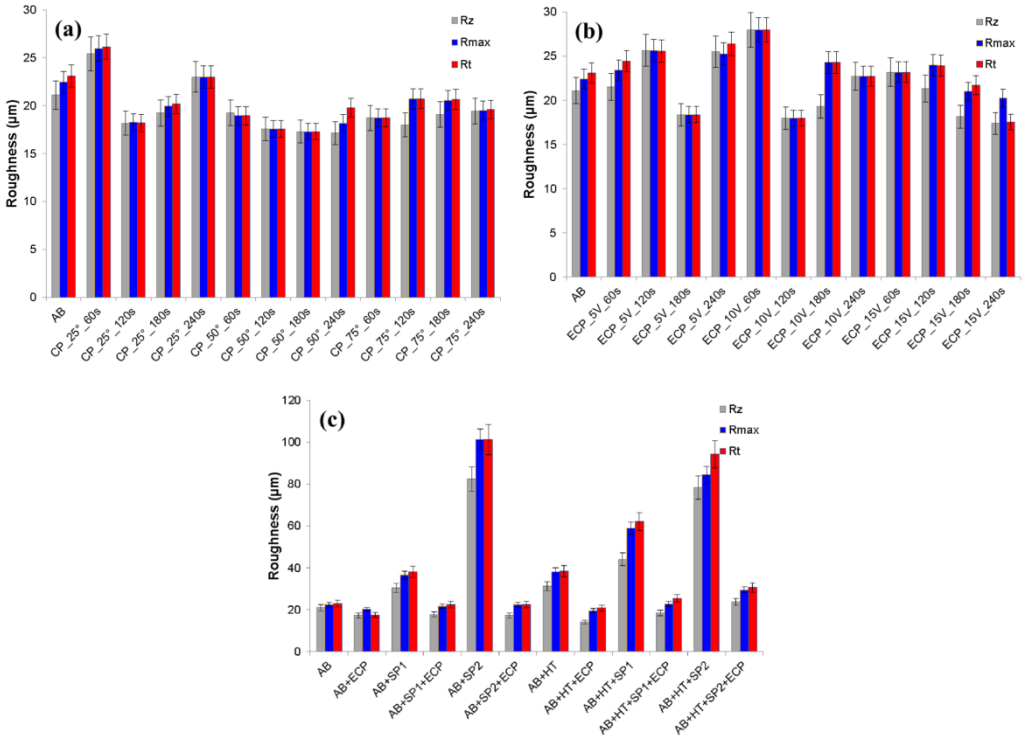

Fig. A. Surface roughness in terms of R_z, R_{max} and R_t for (a) chemical and (b) electro-chemical polishing applied on the as-built samples and (c) electro-chemical polishing of as-built, heat treated and shot peened samples.

Acknowledgement

The authors would like to thank Dr. Davide Mombelli for his valuable helps with the heat treatment. The financial support of Peen Service Srl, for funding the Ph.D. Scholarship of EM, is gratefully appreciated. In addition, the authors appreciate the supports of Martina Riccio from Beam-IT Spa for her worthwhile helps in preparation of the LPBF samples.

Conflict of interest

The authors declare no conflict of interests in this work.

References

[1] I. Yadroitsev, I. Smurov, Surface morphology in selective laser melting of metal powders, in: Phys. Procedia, 2011. https://doi.org/10.1016/j.phpro.2011.03.034.

[2] D. Herzog, V. Seyda, E. Wycisk, C. Emmelmann, Additive manufacturing of metals, Acta Mater. (2016). https://doi.org/10.1016/j.actamat.2016.07.019.

[3] P. Ferro, A. Fabrizi, F. Berto, G. Savio, R. Meneghello, S. Rosso, Defects as a root cause of fatigue weakening of additively manufactured AlSi10Mg components, Theor. Appl. Fract. Mech. (2020). https://doi.org/10.1016/j.tafmec.2020.102611.

[4] B.J. Mfusi, N.R. Mathe, L.C. Tshabalala, P.A.I. Popoola, The effect of stress relief on the mechanical and fatigue properties of additively manufactured AlSi10Mg parts, Metals (Basel). (2019). https://doi.org/10.3390/met9111216.

[5] T. Mukherjee, W. Zhang, T. DebRoy, An improved prediction of residual stresses and distortion in additive manufacturing, Comput. Mater. Sci. (2017). https://doi.org/10.1016/j.commatsci.2016.10.003.

[6] M. Hamidi Nasab, D. Gastaldi, N.F. Lecis, M. Vedani, On morphological surface features of the parts printed by selective laser melting (SLM), Addit. Manuf. (2018).

https://doi.org/10.1016/j.addma.2018.10.011.
[7] S.M. Yusuf, M. Hoegden, N. Gao, Effect of sample orientation on the microstructure and microhardness of additively manufactured AlSi10Mg processed by high-pressure torsion, Int. J. Adv. Manuf. Technol. (2020). https://doi.org/10.1007/s00170-019-04817-5.
[8] W.J. Sames, F.A. List, S. Pannala, R.R. Dehoff, S.S. Babu, The metallurgy and processing science of metal additive manufacturing, Int. Mater. Rev. (2016). https://doi.org/10.1080/09506608.2015.1116649.
[9] S.M. Yusuf, N. Gao, Influence of energy density on metallurgy and properties in metal additive manufacturing, Mater. Sci. Technol. (United Kingdom). (2017). https://doi.org/10.1080/02670836.2017.1289444.
[10] Z. Zhang, C. Sun, X. Xu, L. Liu, Surface quality and forming characteristics of thin-wall aluminium alloy parts manufactured by laser assisted MIG arc additive manufacturing, Int. J. Light. Mater. Manuf. (2018). https://doi.org/10.1016/j.ijlmm.2018.03.005.
[11] R. Li, J. Liu, Y. Shi, L. Wang, W. Jiang, Balling behavior of stainless steel and nickel powder during selective laser melting process, Int. J. Adv. Manuf. Technol. (2012). https://doi.org/10.1007/s00170-011-3566-1.
[12] E. Maleki, S. Bagherifard, M. Guagliano, Application of artificial intelligence to optimize the process parameters effects on tensile properties of Ti-6Al-4V fabricated by laser powder-bed fusion, Int. J. Mech. Mater. Des. (2021). https://doi.org/10.1007/s10999-021-09570-w.
[13] N.T. Aboulkhair, M. Simonelli, L. Parry, I. Ashcroft, C. Tuck, R. Hague, 3D printing of Aluminium alloys: Additive Manufacturing of Aluminium alloys using selective laser melting, Prog. Mater. Sci. (2019). https://doi.org/10.1016/j.pmatsci.2019.100578.
[14] A.H. Maamoun, Y.F. Xue, M.A. Elbestawi, S.C. Veldhuis, The effect of selective laser melting process parameters on the microstructure and mechanical properties of Al6061 and AlSi10Mg alloys, Materials (Basel). (2018). https://doi.org/10.3390/ma12010012.
[15] A.H. Maamoun, Y.F. Xue, M.A. Elbestawi, S.C. Veldhuis, Effect of selective laser melting process parameters on the quality of al alloy parts: Powder characterization, density, surface roughness, and dimensional accuracy, Materials (Basel). (2018). https://doi.org/10.3390/ma11122343.
[16] T. Yang, T. Liu, W. Liao, E. MacDonald, H. Wei, X. Chen, L. Jiang, The influence of process parameters on vertical surface roughness of the AlSi10Mg parts fabricated by selective laser melting, J. Mater. Process. Technol. (2019). https://doi.org/10.1016/j.jmatprotec.2018.10.015.
[17] N.E. Uzan, S. Ramati, R. Shneck, N. Frage, O. Yeheskel, On the effect of shot-peening on fatigue resistance of AlSi10Mg specimens fabricated by additive manufacturing using selective laser melting (AM-SLM), Addit. Manuf. (2018). https://doi.org/10.1016/j.addma.2018.03.030.
[18] A. Leon, E. Aghion, Effect of surface roughness on corrosion fatigue performance of AlSi10Mg alloy produced by Selective Laser Melting (SLM), Mater. Charact. (2017). https://doi.org/10.1016/j.matchar.2017.06.029.
[19] S. Beretta, M. Gargourimotlagh, S. Foletti, A. du Plessis, M. Riccio, Fatigue strength assessment of “as built” AlSi10Mg manufactured by SLM with different build orientations, Int. J. Fatigue. (2020). https://doi.org/10.1016/j.ijfatigue.2020.105737.
[20] J.J. Lewandowski, M. Seifi, Metal Additive Manufacturing: A Review of Mechanical Properties, Annu. Rev. Mater. Res. (2016). https://doi.org/10.1146/annurev-matsci-070115-032024.
[21] A.R. Balachandramurthi, J. Moverare, N. Dixit, R. Pederson, Influence of defects and as-built surface roughness on fatigue properties of additively manufactured Alloy 718, Mater. Sci. Eng. A. (2018). https://doi.org/10.1016/j.msea.2018.08.072.
[22] J. Fiocchi, A. Tuissi, P. Bassani, C.A. Biffi, Low temperature annealing dedicated to AlSi10Mg selective laser melting products, J. Alloys Compd. (2017). https://doi.org/10.1016/j.jallcom.2016.12.019.
[23] M. Tang, P.C. Pistorius, Oxides, porosity and fatigue performance of AlSi10Mg parts produced by selective laser melting, Int. J. Fatigue. (2017). https://doi.org/10.1016/j.ijfatigue.2016.06.002.

[24] J.W. Pegues, S. Shao, N. Shamsaei, N. Sanaei, A. Fatemi, D.H. Warner, P. Li, N. Phan, Fatigue of additive manufactured Ti-6Al-4V, Part I: The effects of powder feedstock, manufacturing, and post-process conditions on the resulting microstructure and defects, Int. J. Fatigue. (2020). https://doi.org/10.1016/j.ijfatigue.2019.105358.
[25] J. Gockel, L. Sheridan, B. Koerper, B. Whip, The influence of additive manufacturing processing parameters on surface roughness and fatigue life, Int. J. Fatigue. 124 (2019) 380–388. https://doi.org/10.1016/j.ijfatigue.2019.03.025.
[26] E. Maleki, O. Unal, K.R.K.R. Kashyzadeh, Effects of conventional, severe, over, and re-shot peening processes on the fatigue behavior of mild carbon steel, Surf. Coatings Technol. 344 (2018) 62–74. https://doi.org/10.1016/j.surfcoat.2018.02.081.
[27] E. Maleki, O. Unal, K. Reza Kashyzadeh, Fatigue behavior prediction and analysis of shot peened mild carbon steels, Int. J. Fatigue. 116 (2018) 48–67. https://doi.org/10.1016/j.ijfatigue.2018.06.004.
[28] E. Maleki, O. Unal, M. Guagliano, S. Bagherifard, Analysing the Fatigue Behaviour and Residual Stress Relaxation of Gradient Nano-structured 316L Steel Subjected to the Shot Peening via Deep Learning Approach, Met. Mater. Int. (2021). https://doi.org/https://doi.org/10.1007/s12540-021-00995-8.
[29] E. Maleki, S. Bagherifard, M. Bandini, M. Guagliano, Surface post-treatments for metal additive manufacturing: Progress, challenges, and opportunities, Addit. Manuf. 37 (2021) 101619. https://doi.org/10.1016/j.addma.2020.101619.
[30] S.M. Ahmadi, R. Kumar, E. V. Borisov, R. Petrov, S. Leeflang, Y. Li, N. Tümer, R. Huizenga, C. Ayas, A.A. Zadpoor, V.A. Popovich, From microstructural design to surface engineering: A tailored approach for improving fatigue life of additively manufactured meta-biomaterials, Acta Biomater. (2019). https://doi.org/10.1016/j.actbio.2018.10.043.
[31] G. Pyka, G. Kerckhofs, I. Papantoniou, M. Speirs, J. Schrooten, M. Wevers, Surface roughness and morphology customization of additive manufactured open porous Ti6Al4V structures, Materials (Basel). (2013). https://doi.org/10.3390/ma6104737.
[32] G. Pyka, A. Burakowski, G. Kerckhofs, M. Moesen, S. Van Bael, J. Schrooten, M. Wevers, Surface modification of Ti6Al4V open porous structures produced by additive manufacturing, Adv. Eng. Mater. (2012). https://doi.org/10.1002/adem.201100344.
[33] F. Scherillo, Chemical surface finishing of AlSi10Mg components made by additive manufacturing, Manuf. Lett. (2019). https://doi.org/10.1016/j.mfglet.2018.12.002.
[34] P. Tyagi, T. Goulet, C. Riso, R. Stephenson, N. Chuenprateep, J. Schlitzer, C. Benton, F. Garcia-Moreno, Reducing the roughness of internal surface of an additive manufacturing produced 316 steel component by chempolishing and electropolishing, Addit. Manuf. (2019). https://doi.org/10.1016/j.addma.2018.11.001.
[35] B. Wysocki, J. Idaszek, J. Buhagiar, K. Szlązak, T. Brynk, K.J. Kurzydłowski, W. Święszkowski, The influence of chemical polishing of titanium scaffolds on their mechanical strength and in-vitro cell response, Mater. Sci. Eng. C. (2019). https://doi.org/10.1016/j.msec.2018.04.019.
[36] A.G. Demir, B. Previtali, Additive manufacturing of cardiovascular CoCr stents by selective laser melting, Mater. Des. (2017). https://doi.org/10.1016/j.matdes.2017.01.091.
[37] J.H. Jung, H.K. Park, B.S. Lee, J. Choi, B. Seo, H.K. Kim, G.H. Kim, H.G. Kim, Study on surface shape control of pure Ti fabricated by electron beam melting using electrolytic polishing, Surf. Coatings Technol. (2017). https://doi.org/10.1016/j.surfcoat.2017.05.061.
[38] E. Maleki, S. Bagherifard, O. Unal, M. Bandini, G.H. Farrahi, M. Guagliano, Introducing gradient severe shot peening as a novel mechanical surface treatment, Sci. Rep. 11 (2021) 22035. https://doi.org/10.1038/s41598-021-01152-2.
[39] B. AlMangour, J.M. Yang, Improving the surface quality and mechanical properties by shot-peening of 17-4 stainless steel fabricated by additive manufacturing, Mater. Des. (2016). https://doi.org/10.1016/j.matdes.2016.08.037.
[40] A. Maamoun, M. Elbestawi, S. Veldhuis, Influence of Shot Peening on AlSi10Mg Parts Fabricated

by Additive Manufacturing, J. Manuf. Mater. Process. (2018). https://doi.org/10.3390/jmmp2030040.
[41] H. Soyama, Y. Okura, The use of various peening methods to improve the fatigue strength of titanium alloy Ti6Al4V manufactured by electron beam melting, AIMS Mater. Sci. (2018). https://doi.org/10.3934/MATERSCI.2018.5.1000.
[42] M. Sato, O. Takakuwa, M. Nakai, M. Niinomi, F. Takeo, H. Soyama, Using Cavitation Peening to Improve the Fatigue Life of Titanium Alloy Ti-6Al-4V Manufactured by Electron Beam Melting, Mater. Sci. Appl. (2016). https://doi.org/10.4236/msa.2016.74018.
[43] M. Benedetti, V. Fontanari, M. Bandini, F. Zanini, S. Carmignato, Low- and high-cycle fatigue resistance of Ti-6Al-4V ELI additively manufactured via selective laser melting: Mean stress and defect sensitivity, Int. J. Fatigue. 107 (2018) 96–109. https://doi.org/10.1016/j.ijfatigue.2017.10.021.
[44] M. Benedetti, E. Torresani, M. Leoni, V. Fontanari, M. Bandini, C. Pederzolli, C. Potrich, The effect of post-sintering treatments on the fatigue and biological behavior of Ti-6Al-4V ELI parts made by selective laser melting, J. Mech. Behav. Biomed. Mater. 71 (2017) 295–306. https://doi.org/10.1016/j.jmbbm.2017.03.024.
[45] E. Salvati, A.J.G. Lunt, S. Ying, T. Sui, H.J. Zhang, C. Heason, G. Baxter, A.M. Korsunsky, Eigenstrain reconstruction of residual strains in an additively manufactured and shot peened nickel superalloy compressor blade, Comput. Methods Appl. Mech. Eng. (2017). https://doi.org/10.1016/j.cma.2017.03.005.
[46] B. AlMangour, J.M. Yang, Integration of Heat Treatment with Shot Peening of 17-4 Stainless Steel Fabricated by Direct Metal Laser Sintering, JOM. (2017). https://doi.org/10.1007/s11837-017-2538-9.
[47] E. Maleki, O. Unal, Shot Peening Process Effects on Metallurgical and Mechanical Properties of 316 L Steel via: Experimental and Neural Network Modeling, Met. Mater. Int. (2019). https://doi.org/10.1007/s12540-019-00448-3.
[48] E. Maleki, O. Unal, Fatigue limit prediction and analysis of nano-structured AISI 304 steel by severe shot peening via ANN, Eng. Comput. (2020). https://doi.org/10.1007/s00366-020-00964-6.
[49] E. Maleki, O. Unal, K. Reza Kashyzadeh, Surface layer nanocrystallization of carbon steels subjected to severe shot peening: Analysis and optimization, Mater. Charact. 157 (2019) 109877. https://doi.org/10.1016/j.matchar.2019.109877.
[50] E. Maleki, O. Unal, A. Amanov, Novel experimental methods for the determination of the boundaries between conventional, severe and over shot peening processes, Surfaces and Interfaces. (2018). https://doi.org/10.1016/j.surfin.2018.09.003.
[51] S. Bagherifard, N. Beretta, S. Monti, M. Riccio, M. Bandini, M. Guagliano, On the fatigue strength enhancement of additive manufactured AlSi10Mg parts by mechanical and thermal post-processing, Mater. Des. 145 (2018) 28–41. https://doi.org/10.1016/j.matdes.2018.02.055.
[52] C. Yan, L. Hao, A. Hussein, Q. Wei, Y. Shi, Microstructural and surface modifications and hydroxyapatite coating of Ti-6Al-4V triply periodic minimal surface lattices fabricated by selective laser melting, Mater. Sci. Eng. C. 75 (2017) 1515–1524. https://doi.org/10.1016/j.msec.2017.03.066.
[53] S.M.J. Razavi, B. Van Hooreweder, F. Berto, Effect of build thickness and geometry on quasi-static and fatigue behavior of Ti-6Al-4V produced by Electron Beam Melting, Addit. Manuf. (2020). https://doi.org/10.1016/j.addma.2020.101426.
[54] K. Solberg, F. Berto, Notch-defect interaction in additively manufactured Inconel 718, Int. J. Fatigue. (2019). https://doi.org/10.1016/j.ijfatigue.2018.12.021.
[55] M. Kahlin, H. Ansell, J.J. Moverare, Fatigue behaviour of notched additive manufactured Ti6Al4V with as-built surfaces, Int. J. Fatigue. (2017). https://doi.org/10.1016/j.ijfatigue.2017.04.009.
[56] K. Solberg, F. Berto, The effect of defects and notches in quasi-static and fatigue loading of Inconel 718 specimens produced by selective laser melting, Int. J. Fatigue. (2020).

https://doi.org/10.1016/j.ijfatigue.2020.105637.
[57] T.D. Mclouth, D.B. Witkin, J.R. Lohser, G.E. Bean, S.D. Sitzman, P.M. Adams, J. Yang, R.J. Zaldivar, Elevated Temperature Notch Sensitivity of Inconel 718 Manufactured by Selective Laser Melting, J. Mater. Eng. Perform. (2021). https://doi.org/10.1007/s11665-021-05522-9.
[58] E. Maleki, S. Bagherifard, S.M.J. Razavi, M. Riccio, M. Bandini, A. du Plessis, F. Berto, M. Guagliano, Fatigue behaviour of notched laser powder bed fusion AlSi10Mg after thermal and mechanical surface post-processing, Mater. Sci. Eng. A. 829 (2022) 142145. https://doi.org/10.1016/j.msea.2021.142145.
[59] N.T. Aboulkhair, I. Maskery, C. Tuck, I. Ashcroft, N.M. Everitt, The microstructure and mechanical properties of selectively laser melted AlSi10Mg: The effect of a conventional T6-like heat treatment, Mater. Sci. Eng. A. (2016). https://doi.org/10.1016/j.msea.2016.04.092.
[60] F. Gharavi, K.A. Matori, R. Yunus, N.K. Othman, F. Fadaeifard, Corrosion behavior of Al6061 alloy weldment produced by friction stir welding process, J. Mater. Res. Technol. (2015). https://doi.org/10.1016/j.jmrt.2015.01.007.
[61] ASM International, Heat Treating of Aluminium Alloys, in: ASM Handbook, Vol. 4 Heat Treat., 1991.
[62] SAE International, SAE J443: Procedures for Using Standard Shot Peening Almen Strip, Surf. Veh. Recomm. Pract. (2010).
[63] C.A. Schneider, W.S. Rasband, K.W. Eliceiri, NIH Image to ImageJ: 25 years of image analysis, Nat. Methods. (2012). https://doi.org/10.1038/nmeth.2089.
[64] EN ISO 4287, Geometrical Product Specifications (GPS) - Surface texture: Profile method - Terms, definitions and surface texture parameters, Int. Organ. Stand. (1997).
[65] P.S. Prevey, X-Ray Diffraction Residual Stress Techniques, in: Mater. Charact., 2018. https://doi.org/10.31399/asm.hb.v10.a0001761.
[66] V. Savaria, F. Bridier, P. Bocher, Computational quantification and correction of the errors induced by layer removal for subsurface residual stress measurements, Int. J. Mech. Sci. (2012). https://doi.org/10.1016/j.ijmecsci.2012.07.003.
[67] F. Trevisan, F. Calignano, M. Lorusso, J. Pakkanen, A. Aversa, E.P. Ambrosio, M. Lombardi, P. Fino, D. Manfredi, On the selective laser melting (SLM) of the AlSi10Mg alloy: Process, microstructure, and mechanical properties, Materials (Basel). (2017). https://doi.org/10.3390/ma10010076.
[68] K. Kempen, L. Thijs, J. Van Humbeeck, J.P. Kruth, Mechanical Properties of AlSi10Mg Produced by Selective Laser Melting, in: Phys. Procedia, 2012. https://doi.org/10.1016/j.phpro.2012.10.059.
[69] X. Liu, C. Zhao, X. Zhou, Z. Shen, W. Liu, Microstructure of selective laser melted AlSi10Mg alloy, Mater. Des. (2019). https://doi.org/10.1016/j.matdes.2019.107677.
[70] M. Tang, P.C. Pistorius, S. Narra, J.L. Beuth, Rapid Solidification: Selective Laser Melting of AlSi10Mg, JOM. (2016). https://doi.org/10.1007/s11837-015-1763-3.
[71] P. Wei, Z. Chen, S. Zhang, X. Fang, B. Lu, L. Zhang, Z. Wei, Effect of T6 heat treatment on the surface tribological and corrosion properties of AlSi10Mg samples produced by selective laser melting, Mater. Charact. (2021). https://doi.org/10.1016/j.matchar.2020.110769.
[72] A.H. Maamoun, M. Elbestawi, G.K. Dosbaeva, S.C. Veldhuis, Thermal post-processing of AlSi10Mg parts produced by Selective Laser Melting using recycled powder, Addit. Manuf. (2018). https://doi.org/10.1016/j.addma.2018.03.014.
[73] N.T. Aboulkhair, C. Tuck, I. Ashcroft, I. Maskery, N.M. Everitt, On the Precipitation Hardening of Selective Laser Melted AlSi10Mg, Metall. Mater. Trans. A Phys. Metall. Mater. Sci. (2015). https://doi.org/10.1007/s11661-015-2980-7.
[74] A. Hadadzadeh, B.S. Amirkhiz, J. Li, M. Mohammadi, Columnar to equiaxed transition during direct metal laser sintering of AlSi10Mg alloy: Effect of building direction, Addit. Manuf. (2018). https://doi.org/10.1016/j.addma.2018.08.001.
[75] A. Basak, S. Das, Epitaxy and Microstructure Evolution in Metal Additive Manufacturing, Annu. Rev. Mater. Res. (2016). https://doi.org/10.1146/annurev-matsci-070115-031728.

[76] L. Thijs, K. Kempen, J.P. Kruth, J. Van Humbeeck, Fine-structured aluminium products with controllable texture by selective laser melting of pre-alloyed AlSi10Mg powder, Acta Mater. (2013). https://doi.org/10.1016/j.actamat.2012.11.052.
[77] F. Alghamdi, X. Song, A. Hadadzadeh, B. Shalchi-Amirkhiz, M. Mohammadi, M. Haghshenas, Post heat treatment of additive manufactured AlSi10Mg: On silicon morphology, texture and small-scale properties, Mater. Sci. Eng. A. (2020). https://doi.org/10.1016/j.msea.2020.139296.
[78] M.D. Wadge, B. Turgut, J.W. Murray, B.W. Stuart, R.M. Felfel, I. Ahmed, D.M. Grant, Developing highly nanoporous titanate structures via wet chemical conversion of DC magnetron sputtered titanium thin films, J. Colloid Interface Sci. (2020). https://doi.org/10.1016/j.jcis.2020.01.073.
[79] A. Ramazani, K. Mukherjee, A. Schwedt, P. Goravanchi, U. Prahl, W. Bleck, Quantification of the effect of transformation-induced geometrically necessary dislocations on the flow-curve modelling of dual-phase steels, Int. J. Plast. (2013). https://doi.org/10.1016/j.ijplas.2012.11.003.
[80] J. Kadkhodapour, S. Schmauder, D. Raabe, S. Ziaei-Rad, U. Weber, M. Calcagnotto, Experimental and numerical study on geometrically necessary dislocations and non-homogeneous mechanical properties of the ferrite phase in dual phase steels, Acta Mater. (2011). https://doi.org/10.1016/j.actamat.2011.03.062.
[81] X. Liang, Z. Liu, Q. Wang, B. Wang, X. Ren, Tool wear-induced microstructure evolution in localized deformation layer of machined Ti–6Al–4V, J. Mater. Sci. (2020). https://doi.org/10.1007/s10853-019-04214-z.
[82] C. peng Liu, R. ming Ren, D. yi Liu, X. juan Zhao, C. huan Chen, An EBSD Investigation on the Evolution of the Surface Microstructure of D2 Wheel Steel During Rolling Contact Fatigue, Tribol. Lett. (2020). https://doi.org/10.1007/s11249-020-1277-1.
[83] Y.J. Liu, Z. Liu, Y. Jiang, G.W. Wang, Y. Yang, L.C. Zhang, Gradient in microstructure and mechanical property of selective laser melted AlSi10Mg, J. Alloys Compd. (2018). https://doi.org/10.1016/j.jallcom.2017.11.020.
[84] N. Takata, H. Kodaira, A. Suzuki, M. Kobashi, Size dependence of microstructure of AlSi10Mg alloy fabricated by selective laser melting, Mater. Charact. (2018). https://doi.org/10.1016/j.matchar.2017.11.052.
[85] D.A. Lesyk, V. V. Dzhemelinskyi, S. Martinez, B.N. Mordyuk, A. Lamikiz, Surface Shot Peening Post-processing of Inconel 718 Alloy Parts Printed by Laser Powder Bed Fusion Additive Manufacturing, J. Mater. Eng. Perform. (2021). https://doi.org/10.1007/s11665-021-06103-6.
[86] Z. Bergant, U. Trdan, J. Grum, Effect of high-temperature furnace treatment on the microstructure and corrosion behavior of NiCrBSi flame-sprayed coatings, Corros. Sci. (2014). https://doi.org/10.1016/j.corsci.2014.07.057.
[87] A. Zakay, E. Aghion, Effect of Post-heat Treatment on the Corrosion Behavior of AlSi10Mg Alloy Produced by Additive Manufacturing, JOM. (2019). https://doi.org/10.1007/s11837-018-3298-x.
[88] S.M.J. Razavi, P. Ferro, F. Berto, J. Torgersen, Fatigue strength of blunt V-notched specimens produced by selective laser melting of Ti-6Al-4V, Theor. Appl. Fract. Mech. 97 (2018) 376–384. https://doi.org/10.1016/j.tafmec.2017.06.021.
[89] A. Townsend, N. Senin, L. Blunt, R.K. Leach, J.S. Taylor, Surface texture metrology for metal additive manufacturing: a review, Precis. Eng. (2016). https://doi.org/10.1016/j.precisioneng.2016.06.001.
[90] L. zhi Wang, S. Wang, J. jiao Wu, Experimental investigation on densification behavior and surface roughness of AlSi10Mg powders produced by selective laser melting, Opt. Laser Technol. (2017). https://doi.org/10.1016/j.optlastec.2017.05.006.
[91] M. Simonelli, C. Tuck, N.T. Aboulkhair, I. Maskery, I. Ashcroft, R.D. Wildman, R. Hague, A Study on the Laser Spatter and the Oxidation Reactions During Selective Laser Melting of 316L Stainless Steel, Al-Si10-Mg, and Ti-6Al-4V, Metall. Mater. Trans. A Phys. Metall. Mater. Sci. 46 (2015) 3842–3851. https://doi.org/10.1007/s11661-015-2882-8.

[92] E. Louvis, P. Fox, C.J. Sutcliffe, Selective laser melting of aluminium components, J. Mater. Process. Technol. (2011). https://doi.org/10.1016/j.jmatprotec.2010.09.019.
[93] A. Amanov, Effect of local treatment temperature of ultrasonic nanocrystalline surface modification on tribological behavior and corrosion resistance of stainless steel 316L produced by selective laser melting, Surf. Coatings Technol. (2020). https://doi.org/10.1016/j.surfcoat.2020.126080.
[94] K. Solberg, D. Wan, F. Berto, Fatigue assessment of as-built and heat-treated Inconel 718 specimens produced by additive manufacturing including notch effects, Fatigue Fract. Eng. Mater. Struct. (2020). https://doi.org/10.1111/ffe.13300.
[95] Y. Duan, J. Zhao, J. Chen, G. Bai, A risk matrix analysis method based on potential risk influence: A case study on cryogenic liquid hydrogen filling system, Process Saf. Environ. Prot. (2016). https://doi.org/10.1016/j.psep.2016.03.022.
[96] A.S. Markowski, M.S. Mannan, Fuzzy risk matrix, J. Hazard. Mater. (2008). https://doi.org/10.1016/j.jhazmat.2008.03.055.
[97] L. Lu, W. Liang, L. Zhang, H. Zhang, Z. Lu, J. Shan, A comprehensive risk evaluation method for natural gas pipelines by combining a risk matrix with a bow-tie model, J. Nat. Gas Sci. Eng. (2015). https://doi.org/10.1016/j.jngse.2015.04.029.